DOI: 10.1002/chem.200901513

Phenacyl–Thiophene and Quinone Semiconductors Designed for Solution Processability and Air-Stability in High Mobility n-Channel Field-Effect Transistors

Joseph A. Letizia, Scott Cronin, Rocio Ponce Ortiz, Antonio Facchetti,* Mark A. Ratner,* and Tobin J. Marks*[a]

Abstract: Electron-transporting organic semiconductors (n-channel) for field-effect transistors (FETs) that are processable in common organic solvents or exhibit air-stable operation are rare. This investigation addresses both these challenges through rational molecular design and computational predictions of n-channel FET air-stability. A series of seven phenacyl–thiophene-based materials are reported incorporating systematic variations in molecular structure and reduction potential. These compounds are as follows: 5,5‴-bis(perfluorophenylcarbonyl)-2,2′:5′,-2″:5″,2‴-quaterthiophene (**1**), 5,5‴-bis-(phenacyl)-2,2′:5′,2″: 5″,2‴-quaterthiophene (**2**), poly[5,5‴-(perfluorophenac-2-yl)-4′,4″-dioctyl-2,2′:5′,2″:5″,2‴-quaterthiophene) (**3**), 5,5‴-bis(perfluorophenacyl)-4,4‴-dioctyl-2,2′:5′,2″:5″,2‴-quaterthiophene (**4**), 2,7-bis((5-perfluorophenacyl)thiophen-2-yl)-9,10-phenanthrenequinone (**5**), 2,7-bis[(5-phenacyl)thiophen-2-yl]-9,10-phenanthrenequinone (**6**), and 2,7-bis(thiophen-2-yl)-9,10-phenanthrenequinone, (**7**). Optical and electrochemical data reveal that phenacyl functionalization significantly depresses the LUMO energies, and introduction of the quinone fragment results in even greater LUMO stabilization. FET measurements reveal that the films of materials **1**, **3**, **5**, and **6** exhibit n-channel activity. Notably, oligomer **1** exhibits one of the highest μ_e (up to $\approx 0.3\ cm^2 V^{-1} s^{-1}$) values reported to date for a solution-cast organic semiconductor; one of the first n-channel polymers, **3**, exhibits $\mu_e \approx 10^{-6}\ cm^2 V^{-1} s^{-1}$ in spin-cast films ($\mu_e = 0.02\ cm^2 V^{-1} s^{-1}$ for drop-cast **1**:**3** blend films); and rare air-stable n-channel material **5** exhibits n-channel FET operation with $\mu_e = 0.015\ cm^2 V^{-1} s^{-1}$, while maintaining a large $I_{on:off} = 10^6$ for a period greater than one year in air. The crystal structures of **1** and **2** reveal close herringbone interplanar π-stacking distances (3.50 and 3.43 Å, respectively), whereas the structure of the model quinone compound, **7**, exhibits 3.48 Å cofacial π-stacking in a slipped, donor-acceptor motif.

Keywords: phenacyl–thiophene · polymers · quinones · semiconductors

Introduction

The promise of lower-cost, flexible, large-area electronics and unique applications has motivated research in the area of organic electronic materials. Organics offer several key attractions, including low-temperature solution processing, readily tunable molecular/polymeric structures, compatibility with organic substrates, roll-to-roll manufacture and unique mechanical/device properties. These characteristics would be invaluable in applications for which low-cost fabrication, mechanical flexibility, large area coverage, and low-temperature processing are desired, such as, in organic light-emitting diodes,[1] sensors,[2] organic photovoltaics,[3] and organic field-effect transistors (OFETs).[4,5] Organic semiconductors (OSCs) are an essential component of each of these

[a] Dr. J. A. Letizia, S. Cronin, Dr. R. P. Ortiz, Dr. A. Facchetti, Prof. M. A. Ratner, Prof. T. J. Marks
Department of Chemistry and the Materials Research Center
Northwestern University, 2145 Sheridan Road
Evanston, Illinois, 60208 (USA)
Fax: (+1) 847-491-2990
E-mail: a-facchetti@northwestern.edu
ratner@northwestern.edu
t-marks@northwestern.edu

Supporting information for this article is available on the WWW under http://dx.doi.org/10.1002/chem.200901513 and contains the full surface microstructure characterization (SEM, AFM, XRD) data.

applications, yet fundamental scientific questions and materials challenges remain concerning long-range charge transport, processability, and ambient stability, especially for electron transporting (n-channel) OFET materials.[5]

Enabling semiconductor film solution processability, while preserving high carrier mobilities, and n-channel FET ambient stability remain some of the most significant challenges for organic electronics.[5] The solubility issue was initially addressed by simply appending bulky solubilizing substituents to disrupt tight solid-state packing; however, this frequently diminishes π–π overlap, leading to lower carrier mobilities.[6] In response, several new strategies were developed based on either geometrically-designed core substituents, which afford both solubilization and close π–π stacking (e.g., TIPS-substituted-pentacenes, TIPS: 6,13-bis(triisopropylsilylethynyl))[7] or on soluble, thermally labile semiconductor precursors (e.g., pentacene cycloadducts and ester-functionalized oligothiophenes)[8] which can yield excellent hole mobilities on conversion to the semiconductor. Despite these advances, organic film growth mechanisms on inorganic/organic surfaces and why certain organic materials crystallize with the proper film morphology/microstructure for FET transport and others do not, remains mysterious. All that is clear is that the addition of highly lipophilic substituents to conjugated cores promotes the formation of uniform, textured films, which are essential for device performance.[9] Several studies have addressed the importance of gate dielectric surface functionalization, attempting to rationalize the effects of surface energy, roughness, chemistry,[10–12] and more recently, viscoelastic properties,[13] on OSC film growth, morphology, and ultimately carrier mobility patterns. Enhanced OSC film morphology and microstructure can also be achieved using a variety of techniques, including substrate rubbing/alignment layers, magnetic fields, layer-by-layer film deposition, vitrification agents, zone casting, zone refining, and solvent vapor annealing.[14] Promising results have also been achieved using external mechanical forces (shear methods).[15] Very recently, surface functionalization of the metallic contacts[16,17] with organic monolayers, combined with small channel lengths have promoted single-crystal-like morphology for TIPS-pentacene device films, yielding impressive charge transport characteristics.[17] However, it is still very difficult to a priori predict from OSC molecular structures what film morphologies/FET performance parameters will be achieved, and most of the aforementioned studies have involved p-channel semiconductors.

Regarding the second of the aforementioned issues, there are three primary reasons why achieving n-channel OFET transport is far more challenging: 1) To enable efficient n-channel transport, planar π-conjugated cores must be functionalized with strong electron withdrawing groups, yielding flat polar molecules with extremely-large crystal packing affinities and very low solubilities. In one study, the polymer BBL[18] (Figure 1) was solubilized by coordination with Lewis acids, followed by casting and leaching the acid from the films. Very recently, we reported soluble and processable arenedicarboximide-based polymers exhibiting very-high

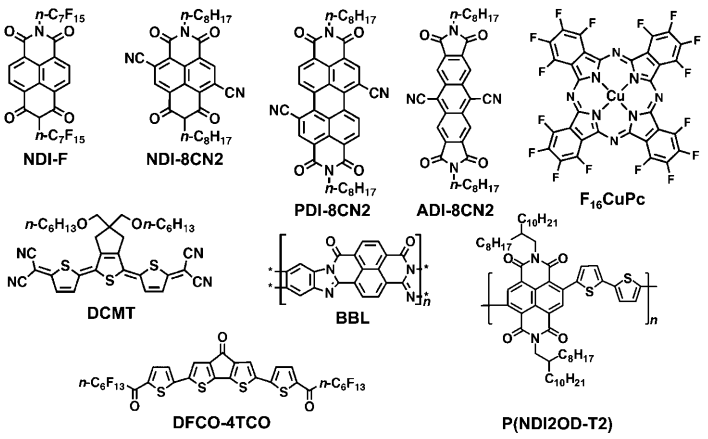

Figure 1. Examples of air-stable organic n-type semiconductors.

electron mobilities.[19] The properties of some of these polymers[19b] are unique and not fully understood at the moment, including the fact that substantial carrier mobilities are exhibited by these nearly amorphous solids. Consequently, a balance between strong electron-withdrawing functionalities, solubilizing groups, local versus molecular/monomeric dipole moments, molecular symmetry, and stacking must be taken into account. 2) Efficient electron injection into the OSC LUMOs requires the use of low workfunction metal contacts; however, the corresponding metal surfaces are then far more reactive than those of high-workfuction noble metals, resulting in the formation of insulating oxide coatings on the former.[20] Furthermore, combining a very-low-workfunction metal with a high-electron-affinity core may result in electrochemical reactions, leading to chemical reaction/dipole formation at the metal-semiconductor interface.[21] Therefore, selection of the most effective contact materials is not obvious for n-channel organic semiconductors. 3) Finally, mobile electron-carrier stabilization in ambient is challenging because of charge trapping by device-born and ambient species.[22–25]

Initial studies addressing the ambient sensitivity of n-channel FETs by de Leeuw et al. argued that ambient atmosphere H_2O and O_2 can trap electron charge carriers, and it was postulated that OSCs with a reduction potential more negative than $\approx$-0.66 V vs. SCE are susceptible to H_2O oxidation.[23] Recent work has revealed that, for several materials, a reduction potential more positive than $\approx -0.2 \pm 0.1$ V vs. SCE is required to stabilize electron charge carriers in the presence of O_2.[25–26] Typically, electron trapping by these gaseous species does not result in chemical degradation of the semiconductor and is reversed when the devices are subjected to vacuum. Air-stable n-channel FET operation has been achieved by either inhibiting O_2 diffusion to the semiconductor film charge-transporting region[23,27] or by designing a semiconductor architecture that stabilizes mobile electrons sufficiently to render them resistant to O_2 trapping (Figure 1).[23,25,26] A fluorocarbon substituent O_2 barrier model was proposed by Katz, et. al, for an air-stable *N*,*N*′-fluorocarbon substituted naphthalene diimide (NDI-

F),[23,28,29] and has also been shown to be applicable to perfluorinated copper phthalocyanine ($CuF_{16}Pc$)[27,30–35] and to fluoroacyl-substituted oligothiophenes (e.g., DFCO-4TCO).[36] Unfortunately, each of these materials exhibits device performance degradation over the period of hours to days in air. Other materials have achieved n-channel operational stability in air by having a reduction potential near ≈ -0.2 V vs. SCE or greater, although in some cases $I_{on:off}$ is diminished.[26,37] These extremely π-deficient air-stable n-channel molecules are core-cyanated naphthalene diimides (NDI-CN_2), core-cyanated perylene diimides PDI-CN_2,[25a,37] cyanated anthracene diimide ADI-8CN_2,[25b] and dicyanomethylene-substituted terthienoquinoids (DCMTs).[26] Recent work on a solution processed DCMT derivative has yielded the highest μ_e to date for an n-type air-stable material, 0.16 $cm^2V^{-1}s^{-1}$; however, $I_{on:off}=10^3$ is diminished by substantial doping at $V_G=0$ V.[26]

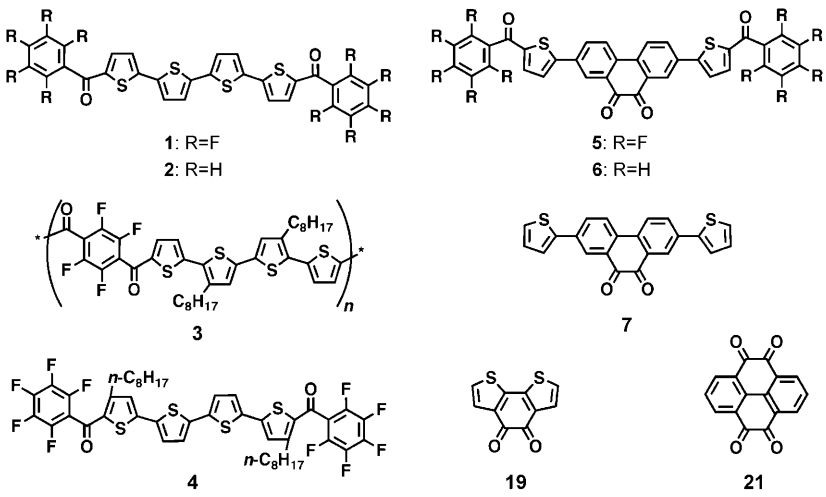

Figure 2. Phenacyl-thiophene and quinone semiconductors and relevant model compounds.

This contribution describes a versatile new class of organic semiconductors designed to enhance crystallinity, solution processability, and achieve air-stable n-channel FET operation. Quaterthiophene is used as the π-core for materials **1**–**4** because of its tendency for favorable crystal packing, generally large carrier mobilities, and amenability to substantial LUMO energy modulation through substituent effects. Previous work on fluorinated and non-fluorinated alkyl,[38–43] aryl,[44] and alkyl-carbonyl[36] substituted thiophenes revealed that high FET carrier mobility can be achieved while stabilizing LUMO energies to enable n-channel FET operation. In the present study, phenacyl substituents are appended to this quaterthiophene π-core to introduce four important characteristics: 1) Enhanced solubility through symmetry-breaking induced by the large phenyl-planar π-core dihedral angle, 2) enhanced crystallinity derived from (perfluoro) phenyl-(perfluoro) phenyl π-stacking, 3) more positive reduction potential resulting from LUMO stabilization by phenacyl and optional perfluorophenacyl substitution, 4) enhanced solution phase rheology and processability by extension of the phenacyl oligomer to polymeric structures by means of *para* substitution of the phenacyl ring.

Materials **1**–**3** were previously communicated as having record-setting FET figures of merit for solution-cast oligomeric and polymeric semiconductors (Figure 2).[45] To understand and enhance FET performance further, the effects of alkyl solubilizing group position on solid-state packing in polymer **3** is investigated here by relocating the substituents from the inner to the outer thiophenes in model compound **4**. Additional LUMO stabilization is first investigated using DFT-level computation, revealing that introduction of quinone-based subunits, 2,2′-bithiophene-3,3′-oxalaldehyde (**19**), 9,10-phenanthrenequinone, or pyrene-4,5,9,10-tetraone (**21**), into the core of **1** should lower the reduction potentials to ≈ -0.5 V, -0.4 V, and -0.2 V vs. SCE, respectively. These reduction potentials span the ≈ -0.6 V to ≈ -0.2 V vs. SCE window previously suggested for air-stable n-channel operation in fluorocarbon-substituted OSCs not subject to ambient carrier doping when reduction potentials are $>\approx -0.1$ V. Synthesis and characterization of new compound **7** confirms a cofacial, antiparallel quinone π-stacking motif with a short 3.48 Å π–π interplanar distance. Synthesis and characterization of new oligomers **5** and **6** reveals n-channel FET activity, with **5** having $\mu_e=0.015$ $cm^2V^{-1}s^{-1}$ while maintaining a large $I_{on:off}=10^6$ after greater than one year in air. This family of materials demonstrates that a balance of high-crystallinity and processability can be achieved, and lays the groundwork for incorporating novel, extremely π-electron deficient monomers into polymeric semiconductors.

Experimental Section

Materials: All reagents were purchased from commercial sources and used without further purification unless otherwise noted. Anhydrous diethyl ether and THF were distilled from Na/benzophenone, and toluene was distilled from Na. The Stille reagent 5,5′-bis(tributylstannyl)-2,2′-bithiophene was synthesized according to a published procedure.[46] Materials 5,5‴-bis(perfluorophenylcarbonyl)-2,2′:5′,2″:5″,2‴-quaterthiophene (**1**), 5,5‴-bis(phenylcarbonyl)-2,2′:5′,2″:5″,2‴-quaterthiophene (**2**), poly-[5,5‴-(perfluorophenac-2-yl)-4′,4″-dioctyl-2,2′:5′,2″ :5″,2‴-quaterthiophene) (**3**), (5-bromothien-2-yl)(perfluorophenyl)methanone (**13**), and (5-bromothien-2-yl)(phenyl)methanone (**14**) were synthesized according to literature procedures.[45] Conventional Schlenk techniques were used and reactions were carried out under N_2 unless otherwise noted. Microwave-assisted reactions were run in sealed vessels using a CEM Discover microwave reactor in the temperature-controlled mode. Optical spectra were recorded by using a Cary Model 1 UV/Visible spectrophotometer. NMR spectra were recorded by using a Varian Unity Plus 500 spectrometer (^{1}H, 500 MHz). Electrochemistry was performed by using a C3 Cell Stand electrochemical station equipped with BAS Epsilon software (Bioanalytical Systems, Inc., Lafayette, IN).

Synthesis of 2-bromo-3-octylthiophene (8): NBS (9.00 g, 50.6 mmol) was added to a solution of 3-octylthiophene (9.93 g, 50.6 mmol) in 22 mL glacial acetic acid maintained at 15 °C. After allowing the reaction mixture to stir for 2 h, it was poured into 200 mL hexane and extracted four times with 50 mL of water, once with 50 mL $NaHSO_4$ (aq, 5% w/v), once with 50 mL brine, and dried over $MgSO_4$. Upon filtration and concentration, 13.7 g of colorless oil **8** was obtained (98% yield) and was used without further purification. Elemental analysis (%) calcd $C_{12}H_{19}BrS$: C, 52.36; H, 6.96; found: C, 52.28; H, 7.05; ^{1}H NMR ($CDCl_3$): $\delta = 7.19$ (d, $J = 4.0$ Hz, 1H), 6.87 (d, $J = 4.5$ Hz, 1H), 2.63 (t, $J = 5.0$ Hz, 2H), 1.60 (t, $J = 5.0$ Hz, 2H), 1.2–1.3 (b, 10H), 0.89 ppm (t, $J = 7.5$ Hz, 3H); MS (EI): m/z (%): 274.0 (100) [M^+].

Synthesis of 3-octylthiophene-2-carboxaldehyde (9): Reagent **8** (30 g, 0.109 mol) was slowly added to Mg turnings (5.3 g, 0.22 mol) while vigorously stirring in 120 mL dry THF in a round bottom flask with attached reflux condenser. The reaction mixture was next heated at reflux for 4 h before it was allowed to cool, filtered through a 0.45 μm syringe filter into a second dry flask, where DMF (0.28 mol, 20 g) was added, and the reaction mixture then refluxed overnight. Once cooled, the reaction mixture was poured into 600 mL hexane, extracted six times with 150 mL of water, and dried over $MgSO_4$. The oil obtained after filtration and concentration was purified by column chromatography on silica gel to give 11.7 g colorless oil (48% yield). Elemental analysis (%) calcd $C_{13}H_{20}OS$: C, 69.59; H, 8.98; found: C, 69.52; H, 8.79; ^{1}H NMR ($CDCl_3$): $\delta = 10.04$ (s, 1H), 7.65 (d, $J = 4.0$ Hz, 1H), 7.02 (d, $J = 4.5$ Hz, 1H), 2.97 (t, $J = 5.0$ Hz, 2H), 1.67 (t, $J = 5.0$ Hz, 2H), 1.2–1.4 (b, 10H), 0.90 ppm (t, $J = 7.5$ Hz, 3H); MS (EI): m/z (%): 224.2 (100) [M^+].

Synthesis of (3-octylthien-2-yl)(perfluorophenyl)methanol (10): A solution of pentafluorobenzene (4.38 g, 26.0 mmol) in 250 mL dry THF was cooled to −78 °C before *n*BuLi (1.6 M in hexanes, 17.9 mL, 28.6 mmol) was added over 15 min. The reaction mixture was maintained at −78 °C for 2 h before **9** (5.83 g, 26.0 mmol) was added and the reaction mixture allowed to stir for another 6 h at −78 °C before being quenched with 20 mL 5% HCl (aq) (CAUTION: Allowing the lithium derivative of pentafluorobenzene to warm to room temperature can result in formation of a potentially explosive benzyne). The reaction mixture was then poured into 300 mL hexane and extracted three times with 50 mL of water, once with 50 mL brine, and dried over $MgSO_4$. The oil obtained after filtration and concentration was purified by column chromatography on silica gel to give 7.91 g of a colorless oil (77% yield). Elemental analysis (%) calcd $C_{19}H_{21}F_5OS$: C, 58.15; H, 5.39; found: C, 58.03; H, 5.36; ^{1}H NMR ($CDCl_3$): $\delta = 7.23$ (d, $J = 4.5$ Hz, 1H), 6.89 (d, $J = 4.5$ Hz, 1H), 6.46 (s, 1H), 2.62 (t, $J = 5.5$ Hz, 2H), 1.2–1.4 (b, 12H), 0.90 ppm (t, $J = 7.5$ Hz, 3H); MS (EI): m/z (%): 392.1 (100) [M^+].

Synthesis of (5-bromo-3-octylthien-2-yl)(perfluorophenyl)methanol (11): NBS (3.41 g, 19.1 mmol) was added in a single amount to a solution of alcohol **10** (7.51 g, 19.1 mmol) in 150 mL glacial acetic acid and allowed to stir overnight. The reaction mixture was then poured into 300 mL hexane and extracted four times with 50 mL of water, once with 50 mL $NaHSO_4$ (aq, 5% w/v), once with 50 mL brine, and dried over $MgSO_4$. Upon filtration and concentration, 9.03 g of a colorless oil was obtained (98% yield) and used without further purification. Elemental analysis (%) calcd $C_{19}H_{19}BrF_5OS$: C, 48.42; H, 4.28; found: C, 48.35; H, 4.31; ^{1}H NMR ($CDCl_3$): $\delta = 6.81$ (s, 1H), 6.38 (s, 1H), 2.62 (t, $J = 5.5$ Hz, 2H), 1.2–1.4 (b, 12H), 0.90 ppm (t, $J = 7.5$ Hz, 3H); MS (EI): m/z (%): 469.9 (100) [M^+].

Synthesis of (5-bromo-3-octylthien-2-yl)(perfluorophenyl)methanone (12): MnO_2 (12 g) was suspended in a solution of alcohol **11** (8.99 g, 19.1 mmol) in 100 mL dichloromethane with stirring for 3 days. After removal of solids by filtration and concentration, the oil was purified by column chromatography on silica gel to give 8.52 g of a colorless oil (94% yield). Elemental analysis (%) calcd $C_{19}H_{18}BrF_5OS$: C, 48.42; H, 4.28; found: C, 48.35; H, 4.31; ^{1}H NMR ($CDCl_3$): $\delta = 7.09$ (s, 1H), 2.95 (t, $J = 6.0$ Hz, 2H), 1.2–1.4 (b, 12H), 0.89 ppm (t, $J = 7.5$ Hz, 3H); MS (EI): m/z (%): 467.9 (100) [M^+].

Synthesis of 5,5‴-bis(perfluorophenacyl)-4,4‴-dioctyl-2,2′:5′,2″:5″,2‴-quaterthiophene (4): A mixture of **12** (0.671 g, 1.43 mmol), 5,5′-bis(tributylstannyl)-2,2′-dithiophene (0.532 g, 0.715 mmol), and tetrakis(triphenylphosphine)palladium(0) (25.0 mg, 0.0215 mmol) was degassed with nitrogen/vacuum three times before 8 mL of anhydrous DMF was added. The reaction mixture was then heated to 80 °C for 10 h with stirring. Upon cooling, the reaction mixture was poured into 100 mL ether and extracted three times with 50 mL of water, once with 50 mL brine, and dried over $MgSO_4$. The red solid obtained upon filtration and concentration was purified by column chromatography on silica gel to give 0.185 g of **4** as a red solid (36% yield). Elemental analysis (%) calcd $C_{30}H_6F_{10}O_2S_4$: C, 50.28; H, 0.84; found: C, 50.14; H, 0.87; ^{1}H NMR ($CDCl_3$): $\delta = 7.20$ (d, $J = 4.5$ Hz, 2H), 7.18 (s, 2H), 7.15 (d, $J = 5.0$ Hz, 2H), 2.96 (t, $J = 8.5$ Hz, 4H), 1.64 (m, 4H), 1.2–1.4 (b, 10H), 0.85 ppm (t, $J = 8.5$ Hz, 6H); m.p. 52–55 °C; MS (EI): m/z (%): 715.8 (100) [M^+].

Synthesis of 5-(5-(pinacolatoboryl)thien-2-yl)(perfluorophenyl)methanone (15): An 8 mL microwave reaction vessel was charged with (5-bromothien-2-yl)(perfluorophenyl)methanone **13** (0.536 g, 1.5 mmol), bis(pinacolato)diboron (0.419 g, 1.65 mmol), [Pd(dppf)Cl_2] (37 mg, 0.045 mmol), and powdered dry potassium acetate (0.442 g, 4.5 mmol) before it was evacuated and refilled with nitrogen four times, and 5 mL toluene added. The reaction mixture was then irradiated with microwaves for 30 min at a temperature of 150 °C. This procedure was repeated five more times and the combined reaction mixtures poured into 30 mL of ether, passed through a 3 cm plug of Celite, concentrated in vacuo, and the resulting oil purified by Kugelrohr distillation (50 mT, 170 °C) to give 1.20 g of boronic ester **15** as a colorless solid (33% yield). Elemental analysis (%) calcd $C_{17}H_{14}BF_5O_3S$: C, 50.52; H, 3.49; found: C, 50.47; H, 3.40; ^{1}H NMR ($CDCl_3$): $\delta = 7.98$ (d, $J = 4.0$ Hz, 1H), 7.72 (d, $J = 4.0$ Hz, 1H), 1.38 ppm (s, 12H); m.p. 53–55 °C; MS (EI): m/z (%): 404.08 (100) [M^+].

Synthesis of 5-(5-(pinacolatoboryl)thien-2-yl)(phenyl)methanone (16): An 8 mL microwave reaction vessel was charged with (5-bromothien-2-yl)(phenyl)methanone **14** (0.267 g, 1.00 mmol), bis(pinacolato)diboron (0.279 g, 1.10 mmol), [Pd(dppf)Cl_2] (25 mg, 0.030 mmol), and powdered dry potassium acetate (0.196 g, 2.00 mmol) before it was evacuated and refilled with nitrogen four times and 6 mL toluene added. The reaction mixture was next irradiated with microwaves for 20 min at a temperature of 160 °C. This procedure was repeated two more times and the combined reaction mixtures poured into 30 mL of ether, passed through a 3 cm plug of Celite, concentrated in vacuo, and the resulting dark oil purified by Kugelrohr distillation (50 mT, 190 °C) to give 0.074 g of boronic ester **16** as a light-yellow viscous oil (50% yield). Elemental analysis (%) calcd $C_{17}H_{19}BO_3S$: C, 64.98; H, 6.09; found: C, 64.81; H, 5.98; ^{1}H NMR ($CDCl_3$): $\delta = 7.89$ (d, $J = 6.5$ Hz, 2H), 7.73 (d, $J = 4.0$ Hz, 1H), 7.64 (d, $J = 4.0$ Hz, 1H), 7.60 (t, $J = 7.0$ Hz, 1H), 7.50 (t, $J = 8.0$ Hz, 2H), 1.38 ppm (s, 12H); m.p. 78–81 °C; MS (EI): m/z (%): 314.10 (100) [M^+].

Synthesis of 3,3′,5,5′-tetrabromo-2,2′-bithiophene (17): Bromine (288 g, 1.8 mol) was added slowly over a 1 h period to a stirred solution of 2,2′-bithiophene (60.0 g, 0.361 mol) in 280 mL chloroform containing 120 mL glacial acetic acid in a 1 L round bottom flask fitted with a reflux condenser (CAUTION: Addition of the first two equivalents of bromine produces a strongly exothermic reaction). The mixture was then stirred at reflux for 12 h. Upon cooling to room temperature, a colorless precipitate was isolated by filtration and washed with methanol. The filtrate was then concentrated and a second crop of tan precipitate was collected and washed with methanol. The combined solids were next dissolved in methylene chloride (500 mL), washed four times with 200 mL water, once with 100 mL brine, and dried over anhydrous $MgSO_4$. The organic solution was then filtered, and the solvent removed by evaporation to give 157 g (90% yield) of a colorless powder. ^{1}H NMR ($CDCl_3$): $\delta = 7.06$ ppm (s, 2H).

Synthesis of 3,3′-dibromo-2,2′-bithiophene (18): Zn powder (31.7 g, 0.485 mol) was added in portions to a vigorously stirred refluxing mixture of bithiophene **17** (77.9 g, 0.162 mol) in 400 mL of ethanol containing 40 mL water, 100 mL glacial acetic acid, and 8 mL of 3 M HCl (aq). After refluxing for 2 h, the mixture was filtered hot and upon cooling to 0 °C, yellow crystals were collected by filtration. The crystals were dissolved in diethyl ether, the resulting solution washed three times with 200 mL water, once with 100 mL brine, and dried over anhydrous $MgSO_4$. The solution was then filtered and the solvent removed by evaporation to give 49.4 g (94% yield) of a light-yellow powder. Elemental analysis (%)

calcd $C_8H_4Br_2S_2$: C, 29.65; H, 1.24; found: C, 29.59; H, 1.14; ^{1}H NMR ($CDCl_3$): $\delta = 7.41$ (d, $J = 5.3$ Hz, 2H), 7.09 ppm (d, $J = 5.3$ Hz, 2H).

Synthesis of 2,2′-bithiophene-3,3′-dicarboxaldehyde (19): A solution of bithiophene **18** (8.39 g, 25.9 mmol) in 50 mL THF was added dropwise over 1 h to a stirring solution of *n*BuLi (82.5 mL, 1.6 M in hexanes) in 200 mL THF at −78 °C. The reaction mixture was allowed to stir for an additional 2 h at −78 °C before dry DMF (4.17 g, 57.0 mmol) in 50 mL THF was added dropwise to the reaction mixture over 30 min. The reaction mixture was then allowed to stir for an additional 30 min before it was quenched with 50 mL of 5% HCl (aq), allowed to warm, washed three times with 200 mL water, once with 100 mL brine, and dried over anhydrous $MgSO_4$. The red solid obtained upon filtration and concentration was purified by column chromatography on silica gel to afford 3.19 g of **19** as a red solid that was dried in vacuo and used immediately in the next reaction. Elemental analysis (%) calcd $C_{10}H_6O_2S_2$: C, 54.03; H, 2.72; found: C, 53.90; H, 2.64; ^{1}H NMR ($CDCl_3$): $\delta = 9.86$ (s, 1H), 7.65 (d, $J = 5.5$ Hz, 2H) , 7.50 ppm (d, $J = 5.5$ Hz, 2H); MS (EI): *m*/*z* (%): 222.1 (100) [M^+].

Synthesis of 2,2′-bithiophene-3,3′-oxalaldehyde (20): The precatalyst 3,4-dimethyl-5-(2-hydroxyethyl)thiazolium iodide (1.70 g, 6.74 mmol) was suspended in 180 mL dry DMF before 1,8-diazabicyclo[5.4.0]undec-7-ene (DBU, 1.02 g, 6.70 mmol) was added slowly and the solution allowed to stir for 5 min. Dialdehyde **19** was then added and the reaction mixture allowed to stir for 2 h under nitrogen, before being opened to air and allowed stir overnight. The dark red reaction mixture was then poured into 500 mL of chloroform, extracted 7x with 200 mL of water, once with 200 mL brine, and dried over $MgSO_4$. A dark colored solid was obtained upon filtration and concentration, and was purified by vacuum sublimation to give 4.61 g of **20** (94% yield). Elemental analysis (%) calcd $C_{10}H_4O_2S_2$: C, 54.53; H, 1.83; found: C, 54.48; H, 1.76; ^{1}H NMR ($CDCl_3$): $\delta = 7.62$ (d, $J = 5.0$ Hz, 2H), 7.44 ppm (d, $J = 5.0$ Hz, 2H); m.p. 221–223 °C; MS (EI): *m*/*z* (%): 220.0 (100) [M^+].

Synthesis of 5,5′-diiodo-2,2′-bithiophene-3,3′-carboxalaldehyde (21): N-iodosuccinimide (4.56 g, 20.2 mmol) was slowly added to a suspension of quinone **20** (2.23 g, 10.1 mmol) in 20 mL $BF_3{\cdot}Me_2O$ and allowed to stir under air in a Nalgene beaker for 4 h before being poured into 100 mL of water, filtered, washed with 20 mL $NaHSO_4$ (aq, 5% w/v), and recrystallized from xylenes to give 2.68 g dark purple crystalline material (61% yield). Elemental analysis (%) calcd $C_{10}H_2I_2O_2S_2$: C, 25.44; H, 0.43; found: C, 25.36; H, 0.49; ^{1}H NMR ([D$_6$]DMSO): $\delta = 7.70$ ppm (s, 2H); m.p. 315–318 °C; MS (EI): *m*/*z* (%): 471.8 (100) [M^+].

Synthesis of 2,7-diiodo-9,10-phenanthrenequinone (22): Iodine (14.6 g, 57.5 mmol) and potassium permanganate (10.3 g, 65.0 mmol) were suspended in a mixture of 100 mL glacial acetic acid and 30 mL acetic anhydride that had been stirring for 5 h. The suspension was stirred vigorously with a magnetic stirbar and maintained at 5 °C while H_2SO_4 (aq, conc., 40 mL) was added dropwise (CAUTION: addition of concentrated H_2SO_4 can produce a vigorous exotherm if not performed slowly). The slurry was then allowed to warm to room temperature before phenanthrenequinone (10.4 g, 50.0 mmol) was added and the reaction mixture stirred for 2 days. The solids were next isolated by filtration, washed with 30 mL hexane, 50 mL methanol, 100 mL $NaHSO_4$ (aq, 5% w/v), 50 mL acetone, and then recrystallized from refluxing xylenes to afford 6.31 g orange solid (27% yield). Elemental analysis (%) calcd $C_{14}H_6I_2O_2$: C, 36.55; H, 1.31; found: C, 36.52; H, 1.25; ^{1}H NMR ([D$_6$]DMSO): $\delta = 8.25$ (s, 2H), 8.11 (d, $J = 7.5$ Hz, 2H), 8.10 ppm (d, $J = 8.0$ Hz, 2H); m.p. 302–305 °C; MS (EI): *m*/*z* (%): 459.9 (100) [M^+].

Synthesis of 2,7-bis((5-perfluorophenacyl)thiophen-2-yl)-9,10-phenanthrenequinone (5): A 25 mL Schlenk flask with attached condenser was charged with boronic ester **15** (0.848 g, 2.10 mmol), aryl iodide **22** (0.460 g, 1.00 mmol), [$Pd_2(dba)_3$] (183 mg, 0.200 mmol), tri-*o*-tolylphosphine (122 mg, 0.400 mmol), and was evacuated, then back-filled with nitrogen five times before 13 mL toluene and 3.1 mL Na_2CO_3 (aq, degassed, 1.5 M) were added. The reaction mixture was heated at reflux overnight and the solids collected by filtration upon cooling, washed with 10 mL acetone, 10 mL methanol, and purified by multiple temperature gradient vacuum sublimations to give 0.190 g of **5** as a dark brown crystalline solid (26% yield). Elemental analysis (%) calcd $C_{36}H_{10}F_{10}O_4S_2$: C, 56.85; H, 1.33; found: C, 56.78; H, 1.21; ^{1}H NMR ([D$_6$]DMSO): $\delta = 8.51$ (d, $J = 8.0$ Hz, 2H), 8.40 (s, 2H), 8.27 (d, $J = 7.5$ Hz, 2H), 8.06 (d, $J = 4.0$ Hz, 2H), 8.02 ppm (d, $J = 4.5$ Hz, 2H); m.p. 351–354 °C; MS (EI): *m*/*z* (%): 760.0 (100) [M^+].

Synthesis of 2,7-bis((5-phenacyl)thiophen-2-yl)-9,10-phenanthrenequinone (6): A 25 mL Schlenk flask with attached condenser was charged with boronic ester **16** (0.736 g, 2.34 mmol), aryl iodide **22** (0.513 g, degassed, 1.12 mmol), [$Pd_2(dba)_3$] (428 mg, 0.47 mmol), tri-*o*-tolylphosphine (142 mg, 0.94 mmol), and was evacuated then back-filled with nitrogen 5x before 15 mL toluene and 3.1 mL Na_2CO_3 (aq, 1.5 M) were added. The reaction mixture was heated at reflux overnight and the solids collected by filtration upon cooling, washed with 10 mL acetone, 10 mL methanol, and recrystallized 5x from boiling nitrobenzene to give 0.214 g of **6** as a brown crystalline material (33% yield). Elemental analysis (%) calcd $C_{36}H_{20}O_4S_2$: C, 74.46; H, 3.47; found: C, 74.59; H, 3.58; ^{1}H NMR ([D$_6$]DMSO): $\delta = 8.51$ (d, $J = 8.0$ Hz, 2H), 8.40 (s, 2H), 8.27 (d, $J = 7.5$ Hz, 2H), 8.06 (d, $J = 4.0$ Hz, 2H), 8.02 ppm (d, $J = 4.5$ Hz, 2H); m.p. 312–315 °C; MS (EI): *m*/*z* (%): 580.2 (100) [M^+].

Synthesis of 2,7-bis(thiophen-2-yl)-9,10-phenanthrenequinone (7): A 25 mL Schlenk flask with attached condenser was charged with 4,4,5,5-tetramethyl-2-(thiophen-2-yl)-1,3,2-dioxaborolane (0.441 g, 2.10 mmol), aryl iodide **20** (0.460 g, 1.00 mmol), [$Pd_2(dba)_3$] (183 mg, 0.200 mmol), tri-*o*-tolylphosphine (122 mg, 0.400 mmol), and was evacuated then back-filled with nitrogen 5× before 13 mL toluene and 3.1 mL Na_2CO_3 (aq, 1.5 M) were added. The reaction mixture was next heated at reflux overnight, and the solids collected by filtration upon cooling, washed with 10 mL acetone, 10 mL methanol, and purified by multiple temperature gradient vacuum sublimations to afford 0.145 g of **7** as a dark brown crystalline solid (39% yield). Elemental analysis (%) calcd $C_{22}H_{12}O_2S_2$: C, 70.94; H, 3.25; found: C, 70.87; H, 3.17; ^{1}H NMR ([D$_6$]DMSO): $\delta = 8.35$ (d, $J = 8.0$ Hz, 2H), 8.19 (s, 2H), 8.08 (d, $J = 8.0$ Hz, 2H), 7.76 (d, $J = 3.5$ Hz, 2H), 7.69 (d, $J = 5.0$ Hz, 2H), 7.22 ppm (t, $J = 4.5$ Hz, 2H); m.p. 295–298 °C; MS (EI): *m*/*z* (%): 372.1 (100) [M^+].

Synthesis of pyrene-4,5,9,10-tetraone (23): Sodium metaperiodate (35.1 g, 164 mmol), water (100 mL), and $RuCl_3{\cdot}3H_2O$ (0.498 g, 2.40 mmol) were added to a solution of pyrene (4.05 g, 20.0 mmol) in a mixture of 80 mL dichloromethane and 80 mL acetonitrile. The reaction mixture was heated to 40 °C, allowed to stir overnight, and upon cooling the solids were collected by filtration. The material was recrystallized from xylenes to give 0.632 g **23** as a black crystalline material (15% yield). Elemental analysis (%) calcd $C_{16}H_6O_4$: C, 73.29; H, 2.31; found: C, 73.26; H, 2.28; ^{1}H NMR ($CDCl_3$): $\delta = 8.46$ (d, $J = 3.5$ Hz, 2H), 8.20 (d, $J = 2.0$ Hz, 2H) , 7.82 ppm (d, $J = 8.0$ Hz, 2H); MS (EI): *m*/*z* (%): 262.0 (100) [M^+].

Synthesis of 2,7-diiodopyrene-4,5,9,10-tetraone (24): N-iodosuccinimide (0.674 g, 3.00 mmol) dissolved in 1 mL H_2SO_4 (aq, conc.) was slowly added to a suspension of tetraone **23** (262 mg, 1.00 mmol) in a mixture of 2 mL trifluoroacetic acid and 5 mL H_2SO_4 (aq, conc.). The reaction mixture was allowed to stir for 2 days at 40 °C before being poured into 20 mL of water, filtered, washed with 20 mL $NaHSO_4$ (aq, 5% w/v), and recrystallized from nitrobenzene to give 295 mg of **24** as a black crystalline material (59% yield). Elemental analysis (%) calcd $C_{16}H_4I_2O_4$: C, 37.39; H, 0.78; found: C, 37.27; H, 0.69; ^{1}H NMR ([D$_6$]DMSO): $\delta =$ 8.51 ppm (s, 4H); MS (EI): *m*/*z* (%): 513.9 (100) [M^+].

Polymer molecular weight determination: GPC measurements were performed by using a Polymer Laboratories PL-GPC 220 instrument with 1,2,4-trichlorobenzene as the solvent (stabilized with 125 ppm BHT) at 150 °C. A set of three PLgel 10 μm mixed columns was used. Samples were prepared at 160 °C. Molecular weights were determined by GPC using narrow polystyrene standards and are not corrected.

FET device fabrication and measurement: Prime grade p-doped silicon wafers (100) having 300 nm thermally grown oxide (Process Specialties Inc.) were used as device substrates. These were sonicated in methanol, acetone, propanol, and oxygen plasma cleaned before film deposition. Trimethylsilyl functionalization of the SiO_2 surface was carried out by exposing the cleaned silicon wafers to hexamethyldisilazane (HMDS) vapor under nitrogen at room temperature for 4 days. Vacuum-deposited films of oligomers were thermally evaporated onto temperature-controlled substrates under high-vacuum at a QCM quantified growth rate of 0.1–

0.2 Å/s. Solution-deposited oligomer and oligomer-polymer blend films were drop-cast from 0.4 mL toluene or xylenes solutions onto a temperature-controlled substrate in a solvent-saturated air atmosphere. Films of polymer **3** were spin-coated and drop-cast from a 500 ppm solution in a xylenes/diethylamine mixture (9:1 v/v), dried at 120 °C in vacuo for 12 h, and annealing was performed at 150 °C and 250 °C with negligible enhancement in device performance. For FET device fabrication, top-contact gold electrodes (500 Å) were deposited by thermal evaporation through a shadow mask to define channels with dimensions 100 μm (L) × 2.00 mm (W). The capacitance of the insulator is 1×10^{-8} F cm^{-2} for 300 nm SiO_2, and mobility was measured in the saturation regime. TFT device measurements were carried out at 21–23 °C in a customized probe station under high-vacuum ($<1\times10^{-6}$ Torr) or in air. Coaxial and/or triaxial shielding was incorporated into Signaton probes to minimize the noise level. TFT characterization was performed by using a Keithley 6430 sub-femtoampmeter (drain) and a Keithley 2400 (gate) source meter, operated by a locally written Labview program and GPIB communication. Thin films were analyzed by wide-angle X-ray film diffractometry (WAXRD) on a Rikagu ATX-G instrument using standard $\theta-2\theta$ techniques and Cu$K\alpha_1$ radiation. Scanning electron microscopy was performed by using a Hitachi 4800 SEM with samples having a 2 nm Au/Pd sputtered film.

Electrochemistry: Cyclic voltammetry measurements were performed in an electrolyte solution of 0.1 M tetrabutylammonium hexafluorophosphate in dry THF. Platinum electrodes were used as both working and counter electrodes, and Ag wire was used as the pseudo-reference electrode. A ferrocene/ferrocenium redox couple was used as an internal standard and potentials obtained in reference to the silver electrode were converted to the saturated calomel electrode (SCE) scale.

Thermal characterization: All materials were dried under vacuum for 3 d at 100 °C before thermal analysis. Thermogravimetric analysis (TGA) was performed by using a Mettler Toledo TMA/SDTA841e at a ramp rate of 10 °C min^{-1} using an aluminum oxide crucible under vacuum (5 T) for molecular materials or under nitrogen at atmospheric pressure for the polymer. Differential scanning calorimetry (DSC) was performed by using a Mettler Toledo DSC823e at a ramp rate of 10 °C min^{-1} using aluminum pans under nitrogen.

Computational methodology: Equilibrium geometry optimizations were performed in QChem 2.1[47] at the density functional theory (DFT) level with a B3LYP functional and the 6-31G* basis set. Single point calculations using these geometries were then performed at the DFT/B3LYP/6-31+G* level of theory to obtain molecular orbital energy levels (QChem) and orbital electron density plots (Spartan ′06). Energy levels were calibrated to the experimental HOMO/LUMO energies[39] of sexithiophene.

Single crystal structure determination: Single crystals of **1**, **2**, and **7** were grown by gradient sublimation. X-ray single crystal diffraction measurements were performed on a Bruker CCD area detector instrument with graphite-monochromated Mo$K\alpha$ (0.71073 Å) radiation. The data were collected at 153(2) K, and the structures were solved by direct methods and expanded using Fourier techniques. Crystallographic details for **7** are provided in the Supporting Information; those for **1** and **2** are given elsewhere.[45]

Results

This account begins with a discussion of synthetic strategies and routes to compounds **1**–**7**. Next, molecular and materials characteristics such as optical and electrochemical properties and thermal transitions as determined by UV/Vis/PL spectroscopy, cyclic voltammetry, polarized optical microscopy, and DSC/TGA are outlined. Solid-state microstructures and surface morphologies in the corresponding thin films as investigated by film and single-crystal X-ray diffraction and SEM are then presented. Finally, the charge transport characteristics of the semiconducting films as defined in thin film transistor configurations are discussed in the context of the other physical data.

Synthesis: The syntheses of the present phenacyl semiconductors are outlined in Scheme 1. Compounds **1**–**3** were obtained by Stille coupling of the appropriate phenacyl–thiophene bromide with bis-stannylated bithiophene, as previously reported.[45] Gel permeation chromatography (GPC) was used to determine the molecular weight of polymer **3** versus polystyrene, yielding $M_W=15{,}300$ D and PDI = 2.51. Model compound **4** was likewise obtained by Stille coupling of 5-(5-(pinacolatoboryl)thien-2-yl)(perfluorophenyl)methanone **15** with 5,5′-bis(tributylstannyl)-2,2′-bithiophene. Phenanthrene–quinone-based compounds **5**–**7** were obtained by Suzuki coupling of the corresponding boronic ester and 2,7-diiodophenanthrenequinone (**22**). Purification of **5** and **7** was achieved by multiple gradient sublimation, and **6** was purified by multiple recrystallizations from nitrobenzene. The two other quinine reagents, 5,5′-diiodo-2,2′-bithiophene-3,3′-oxalaldehyde (**21**) and 2,7-diiodopyrene-4,5,9,10-tetraone (**24**) were synthesized in five and two steps, respectively, from commercially available starting materials. Coupling of bithiophene quinone **21** with **15** or with 4,4,5,5-tetramethyl-2-(thiophen-2-yl)-1,3,2-dioxaborolane yields the desired products (confirmed by EI-MS), however the reaction mixtures decompose below 250 °C, precluding product isolation by sublimation, and are intractable (even using refluxing nitrobenzene or trichlorobenzene). Suzuki coupling of boronic ester **15** or 4,4,5,5-tetramethyl-2-(thiophen-2-yl)-1,3,2-dioxaborolane with **24** yielded intractable solids, and the EI-MS spectra of these materials do not indicate the presence of the desired products.

Semiconductor building blocks **12**–**16**, **21**, **22**, and **24** were all synthesized from commercially available starting materials as shown in Scheme 2. The n-octyl-functionalized aryl bromide **12**, precursor to semiconductor **4**, was synthesized in four steps. First, 3-n-octylthiophene is brominated to give **8**, which was then formylated by quenching the Grignard reagent with DMF. The lithium salt of pentafluorobenzene was next reacted with 2-carboxythiophene **9** to afford alcohol **10**, which was brominated with NBS and oxidized with MnO_2 to afford ketone **12**. After purification by means of column chromatography, **12** was coupled with 5,5′-bis(tributylstannyl)-2,2′-bithiophene to yield new oligomer **4** in 36% yield, after purification by column chromatography and Kugelrohr distillation (Scheme 1).

Catalytic borylation[48,49] was employed in the synthesis of intermediates **15** and **16**, precursors to semiconductors **5** and **6**, since both the π-deficient quinone core **22** and the phenacyl–thiophene units in **13** and **14** are unstable under standard metalation conditions. Since borylation and acetal protection of quinones **21** and **22** was unsuccessful, efforts focused on catalytic borylations of the phenacyl–thiophene bromides **13** and **14**. Furthermore, because borylation of **13** performed in the standard solvent DMF[48,50] afforded the

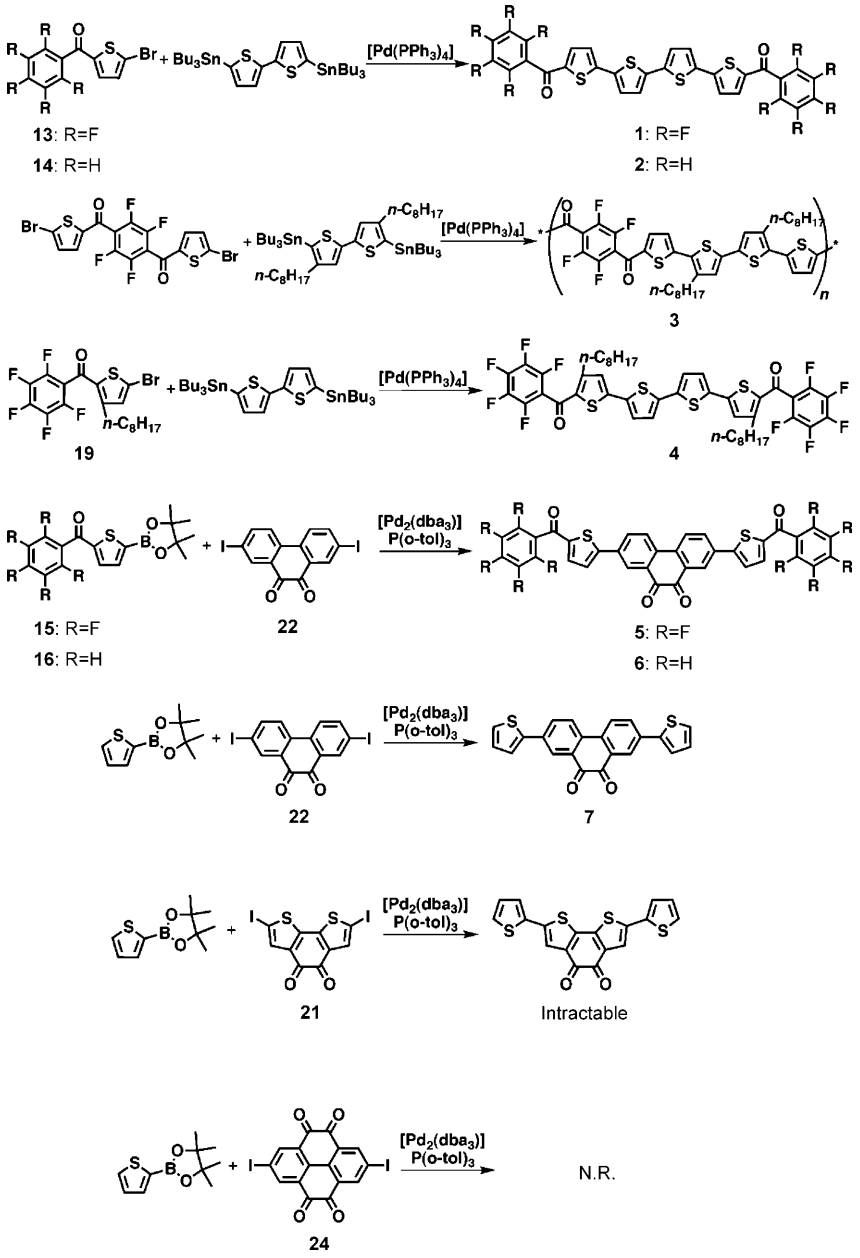

Scheme 1. Synthesis of semiconductors **1**–**7**.

para-hydroxyl substituted pentafluorophenyl derivative, anhydrous toluene was used as the reaction medium. Note that the reactions performed using conventional heating proceeded in low yields (<5% in this case), however, microwave irradiation resulted in yields of 33% and 50% for **15** and **16**, respectively, after purification by Kugelrohr distillation.

Iodo-functionalized quinone core reagents were used here since the corresponding aryl-bromide derivatives were unreactive under Suzuki coupling conditions. Quinone **21** is synthesized in five steps from 2,2′-bithiophene. First, 2,2′-bithiophene was tetrabrominated by refluxing with Br_2 in a mixture of chloroform and acetic acid to give 3,5,3′,5′-tetrabromo-2,2′-bithiophene **17**, which was selectively debrominated with Zn to yield 3,3′-dibromo-2,2′-bithiophene **18**. Reagent 3,3′-dicarboxy-2,2′-bithiophene (**19**) was obtained by slowly adding **18** to a dilute solution of *n*BuLi followed by reacting the dilithium derivative with DMF. The dialdehyde undergoes benzoin condensation[51] in the presence of 3,4-dimethyl-5-(2-hydroxyethyl)thiazolium iodide to give the cyclized α-hydroxy ketone, which was then oxidized in air to afford quinone **20** in 94% yield, after purification by sublimation. Aryl-diiodide **21** was obtained in 61% yield by BF_3·O-$(CH_3)_2$-catalyzed iodination of **20** with *N*-iodo-succinimide. Finally, commercially available phenanthrenequinone was iodinated by $I_2/KMnO_4$ to afford **22** in 27% yield after recrystallization from xylenes. Diiodinated pyrenetetraone **24** is obtained by $RuCl_3$-catalyzed oxidation of pyrene with sodium metaperiodate, followed by iodination with $I_2/KMnO_4$.

Semiconductor thermal properties: Thermogravimetric analysis (TGA) was used to evaluate the thermal stability of semiconductors **1**–**7** (Figure 3a, Table 1). A mass loss of 5% is defined as the threshold for sublimation (**1**, **2**, **5**, **6**, **7**) or decomposition (**3**, **4**). The TGA properties of compounds to be used in film growth by vacuum deposition (**1**, **2**, **5**, **6**, **7**) were measured at a pressure of 5 Torr (N_2), and the TGA of materials only to be processed from solution (**3**, **4**) was performed under N_2 at atmospheric pressure. All of the present molecular materials demonstrate good thermal stability and volatility, with the onset of sublimation at 295 and 342 °C for **1** and **2**, respectively, and at 375, 404 °C, and 309 °C for quinone-based **5**, **6**, and **7**, respectively. Polymer **3** and solution-cast molecule **4** decompose at 425 and 363 °C, respectively. Differential scanning calorimetry (DSC) was employed to study the thermal transitions of **1**–**7** under N_2. DSC plots reveal reversible melting transitions at 294 (**1**), 306 (**2**), 352 (**5**), 316 (**6**), and 297 °C (**7**) for the vacuum-deposited materials (Figure 3b and Table 1).

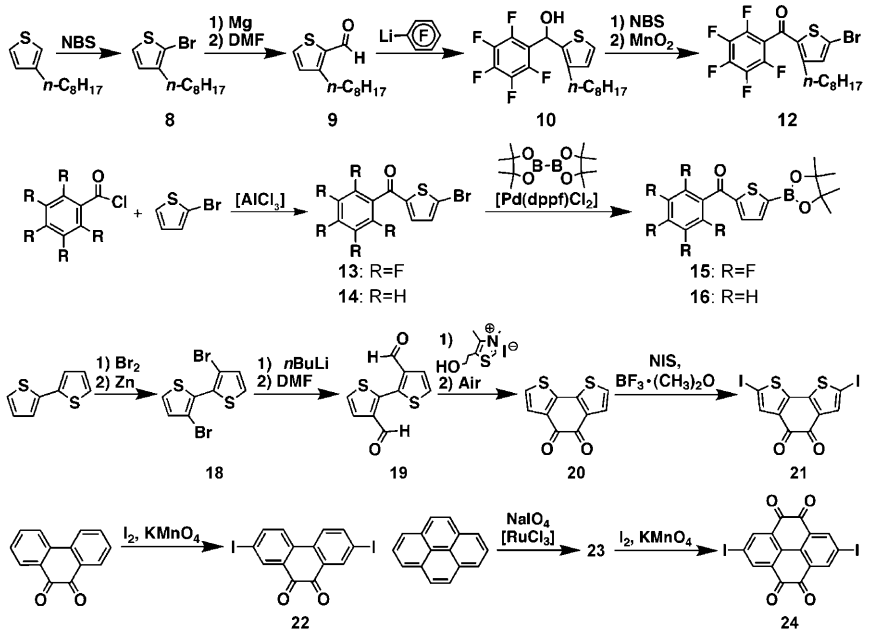

Scheme 2. Synthesis of organic semiconductor precursors.

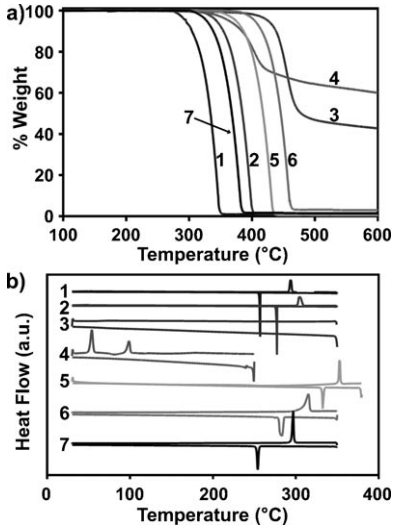

Figure 3. a) Thermogravimetric analysis (TGA) and b) differential scanning calorimetry (DSC) plots of materials **1**–**7**. See Table 1 for data.

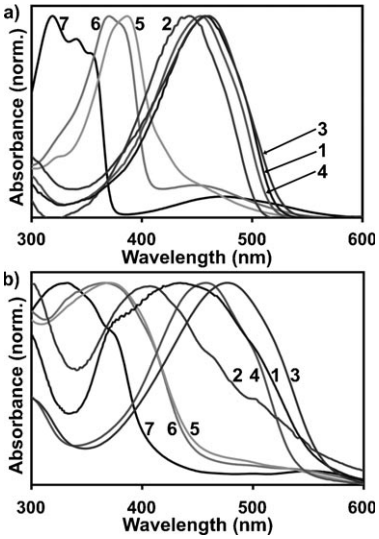

Figure 4. Optical absorption spectra of compounds **1**–**7** in a) THF solution and b) thin films on glass.

Table 1. Thermal properties semiconducting of phenacyl oligomers and polymers

	m.p. [°C]	T_{DSC} [°C]		T_{TGA} [°C]
		Heating	Cooling	
1	291–194	294	257	295
2	302–307	306	277	342
3	–	–	–	425
4	95–99	51, 99	–	363
5	350–353	352	333	375
6	309–316	316	281	404
7	294–297	297	254	309

Polymer **3** exhibits no thermal transitions in the experimental window, while material **4** undergoes a liquid crystalline transition at 51 °C and melting at 99 °C. Thermal data are summarized in Table 1.

Optical properties: Solution and thin-film UV/Visible absorption spectra of the new phenacyl oligomers and polymer **3** are shown in Figure 4, and the optical spectroscopic data summarized in Table 2. In THF solution, molecules **1**, **2**, and polymer **3** exhibit absorption maxima at $\lambda = 458$, 442, and 460 nm, respectively. The spectra of **1** and **2** as thin films reveal hypsochromic shifts of 23 nm and 38 nm, respectively, while the absorption maximum of **3** shifts bathochromically by 16 nm. Compound **4** exhibits behavior similar to that of polymer **3**, with a solution absorption maximum at $\lambda = 453$ nm and a bathochromic shift for the film to $\lambda = 457$ nm. Note that the maxima of Quinone-based materials **5**, **6**, and **7** are significantly blue-shifted, with their solution absorption maxima located at $\lambda = 369$, 370, and 318 nm, respectively. As thin films, these materials exhibit slight peak broadening with absorbtion maxima at $\lambda = 371$, 365, and 329 nm, respectively.

Electrochemical properties: The redox behavior of compounds **1**–**7** was investigated using cyclic voltammetry

Table 2. Summary of optical absorbtion spectroscopic data for materials **1**-**7**.

	λ_{max}^{soln} [nm]	$\lambda_{shoulder}^{soln}$ [nm]	λ_{max}^{film} [nm]	$\lambda_{shoulder}^{film}$ [nm]	E_{gap}^{opt} [a] [eV]	HOMO[b] [eV]	LUMO[c] [eV]
1	458	–	435	495, 373	2.40	5.99	−3.59
2	442	–	404	462	2.47	5.90	−3.43
3	460	–	476	522	2.37	5.72	−3.35
4	453	–	457	469	2.41	5.88	−3.47
5	369	374, 322	371	–	2.62	6.64	−4.03
6	370	382	365	–	2.54	6.56	−4.02
7	318	340, 354	329	370	2.56	6.53	−3.97

[a] Optical band gap calculated from the red edge of the S_0–S_1 absorption band at 1/10 the maximum intensity. [b] HOMO energy estimated by subtracting the optical gap from LUMO energy. [c] Estimated from the onset of the first electrochemical reduction using the correction factor −4.4 V to convert SCE reference to vacuum.[52]

(Figure 5 and Table 3). Oligomers **1** and **2** exhibit onsets of reduction at −0.81 and −0.97 V with first reduction half-wave potentials of −1.03 and −1.31 V, respectively. Two irreversible oxidation events are observed for **1** at +1.07 and +1.22 V, whereas no oxidations are observed for **2**. Polymer **3** exhibits three reversible reductions with onset at −1.05 V and half-wave potentials located at −1.12, −1.24, and −1.79 V. Two irreversible oxidations are observed for **3** at +0.96 and +1.13 V. Interestingly, new model compound **4** exhibits a 0.2 V anodic shift in reduction potential compared to **1**, with onset at −1.16 V and with the reduction half-wave located at −1.23 V. Two irreversible oxidations are also observed for **4** at +1.04 and +1.40 V. The new quinine-containing molecules exhibit significant ≈0.6 V cathodic shifts in their completely reversible reduction behavior. Reduction onset occurs for **5**, **6**, and **7**, respectively at −0.37, −0.39, and −0.43 V; the first half-wave potentials are located at −0.45, −0.46, and −0.54 V; the second half-wave potentials at −1.02, −1.08, and −1.08 V; and the third half-wave potentials at −1.74, −1.82, and −1.37 V. One irreversible oxidation event is observed for **5** at +1.60 V. It is interesting that the quaterthiophene-based materials exhibit a 0.3 V cathodic shift upon fluorination while the quinone-based materials have onset and reduction half-wave potentials that are largely independent of ancillary substitution.

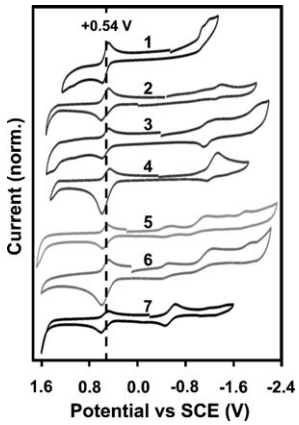

Figure 5. Cyclic voltammograms of materials **1**–**7** in THF solution. Data are collected in Table 3. The dashed line overlaps with the Fc/Fc^+ redox process.

Thin-film X-ray diffraction and surface microstructure analysis: Thin-film wide angle X-ray diffraction (WAXRD) $\theta-2\theta$ scans of films of compounds **1**–**7** were performed to investigate the degree of film crystallinity and molecule/polymer chain orientation with respect to the substrate surface. Scanning electron microscopy (SEM) was employed to characterize film surface morphology and uniformity. Films were vacuum deposited or drop-cast on the same substrates (HMDS treated p^{++}-Si-300 nm SiO_2) used to fabricate TFTs. Thin films of oligomers **1**, **2**, **5**, and **6** exhibit strong Bragg diffraction features (Figure 6), while those of molecules **4**, **7**, and polymer **3** do not exhibit detectable reflections in WAXRD scans. SEM imaging reveals primarily homogenous films with crystallites and ribbons protruding from the surface (Figure 7 and Figure 8).

Thin films of oligomers **1** and **2** exhibit strong Bragg reflections in $\theta-2\theta$ scans up to 10th and 8th order, respectively. The scans indicate single-phase films with *d*-spacings of 26.6±0.1 Å (**1**) and 26.3±0.1 Å (**2**). As the substrate deposition temperature (T_D) increases, higher intensities and narrower reflections are observed for both films. The $\theta-2\theta$ diffraction patterns of quinone-based materials **5** and **6** show similar crystallinity trends with T_D. Oligomer **5** exhibits a single family of Bragg reflections up to 9th order with a *d*-spacing of 27.9±0.1 Å, indicating a single-phase film. Films of **6** exhibit reflections up to 7th order with a primary *d*-spacing of 25.90±0.08 Å, a second phase is also present at T_D= 150 °C having a *d*-spacing of 27.05±0.04 Å.

SEM imaging of vapor-deposited oligomer **1** and **2** films reveals crystallites protruding from a smooth underlying film (Figure 7a–f). Crystallite size increases with T_D for both materials from ≈100 nm at 25 °C to ribbons > 1 μm long at 90 °C. Solution-cast films of **1** exhibit large crystalline plates having

Table 3. Anodic (E_a), cathodic (E_c), and half-wave ($E^{1/2}$) potentials (V vs. SCE) from cyclic voltammetry of semiconductors **1**–**7**.

	Oxidation[a] Cathodic		Reduction Cathodic			Reduction Anodic			Half-wave		
	E_{c1}	E_{c2}	E_{c1}	E_{c2}	E_{c3}	E_{a1}	E_{a2}	E_{a3}	$E_1^{1/2}$	$E_2^{1/2}$	$E_3^{1/2}$
1	1.07	1.22	−0.99	−1.12	–	−1.07	−1.18	–	−1.03	−1.15	–
2	–	–	−1.27	–	–	−1.35	–	–	−1.31	–	–
3	0.96	1.13	−1.08	−1.15	−1.88	−1.17	−1.32	−2.06	−1.12	−1.24	−1.97
4	1.04	1.40	−1.13	–	–	−1.34	–	–	−1.23	–	–
5	1.60	–	−0.40	−0.86	−1.69	−0.50	−1.18	−1.79	−0.45	−1.02	−1.74
6	–	–	−0.41	−0.91	−1.74	−0.51	−1.25	−1.89	−0.46	−1.08	−1.82
7	–	–	−0.44	−1.04	−1.27	−0.64	−1.12	−1.47	−0.54	−1.08	−1.37

[a] Oxidation events were irreversible.

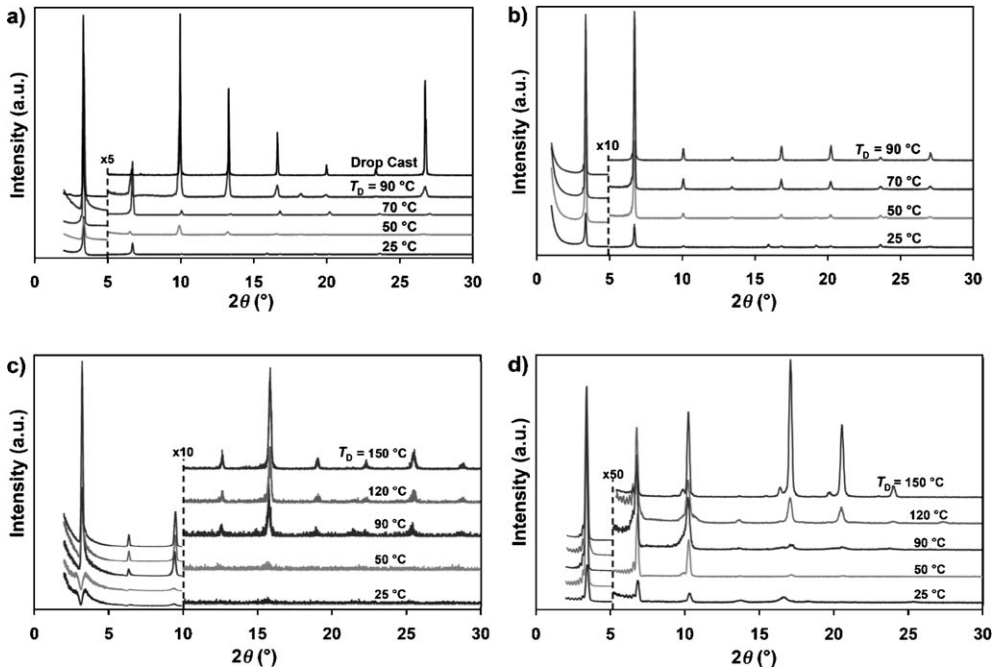

Figure 6. X-ray diffraction θ-2θ plots of semiconductor a) **1**, b) **2**, c) **5**, and d) **6** thin films vapor-deposited (unless otherwise noted) onto Si/SiO_2 substrates temperature controlled at the indicated T_D.

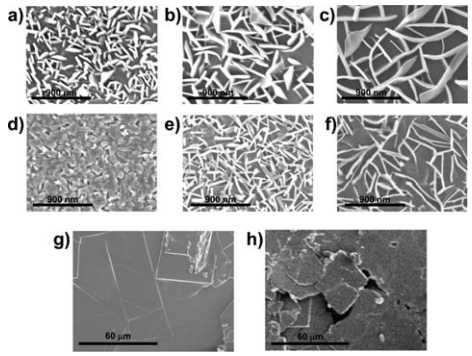

Figure 7. SEM micrographs of semiconductor **1** and **2** thin films vapor-deposited onto temperature-controlled substrates at 25 (a, d), 70 (b, e), or 90 °C (c, f), as well as solution-cast films of **1** (g, toluene, 500 ppm) and a **1**:**3** blend (h, toluene, 1:1, 500 ppm).

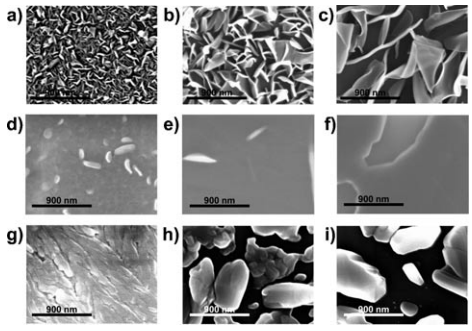

Figure 8. SEM micrographs of semiconductors **5** (a, b, c) and **6** (d, e, f) thin films vapor-deposited onto temperature-controlled Si/SiO_2 substrates at 25 (a, d,), 120 (b, e), or 150 °C (c, f), as well as micrographs of **7** thin films vapor-deposited onto temperature-controlled Si/SiO_2 substrates at 50 (g), 50 (h), or 90 °C (i).

flat surfaces and dimensions $>$ 50 μm in SEM images (Figure 7g) and with birefringence in the optical micrographs (Figure S1a). Blends of oligomer **1** and polymer **3** also exhibit film surfaces with crystal plates having dimensions of $\approx$50 μm in SEM images (Figure 7h) and with birefringence in the optical micrographs (Figure S1b).

SEM imaging of vapor-deposited **5** films reveals surface morphology similar to that of **1** and **2**. Crystallites $\approx$100 nm long dominate the surface of films grown at $T_D = 25$ °C, while longer ribbons $>$ 1 μm protrude from an otherwise smooth film at higher T_D (Figures 8a–c). Oligomer **6** exhibits a surface with fewer crystallites at $T_D = 25$ °C, which grow and coalesce into a smooth film at intermediate T_D before gaps begin to appear in the film at $T_D = 150$ °C (Figure 8d–f). Films of **7**, which do not exhibit detectable X-ray diffraction, also have a markedly different surface morphology from the other materials. Films at $T_D = 25$ °C are amorphous and become discontinuous as T_D increases, with large gaps forming between islands of **7** (Figures 8g–h).

Transistor fabrication and optimization: Thin film transistors were fabricated with films of **1**–**7** as the semiconducting layer. Oligomers **1**, **2** and **4**–**7** were vacuum-deposited (**1**, **2**, and **4** were also drop-cast), while polymer **3** was spin-cast and drop-cast. A minimum of 10 devices for each material was tested under high-vacuum and once fully characterized, their operational stability in ambient air also characterized. Oligomers **1**, **3**, **5**, and **6** exhibit exclusively n-type transport in a top-contact bottom-gate FET geometry (Figures 9, 10, and Figure S2), while OSC **2** exhibits exclusively p-type behavior.

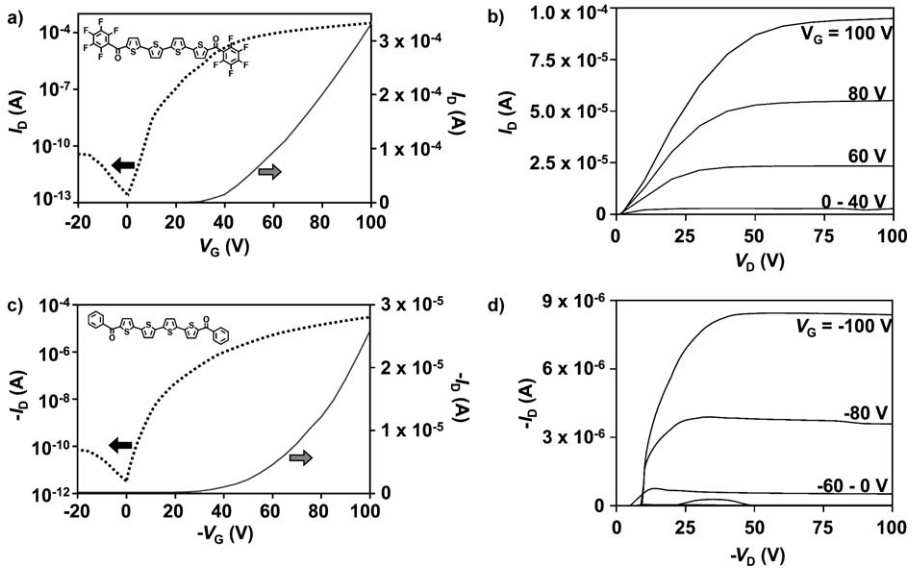

Figure 9. FET transfer (a, c) and output (b, d) plots of vacuum-deposited films of **1** (T_D = 80 °C) and **2** (T_D = 90 °C), respectively.

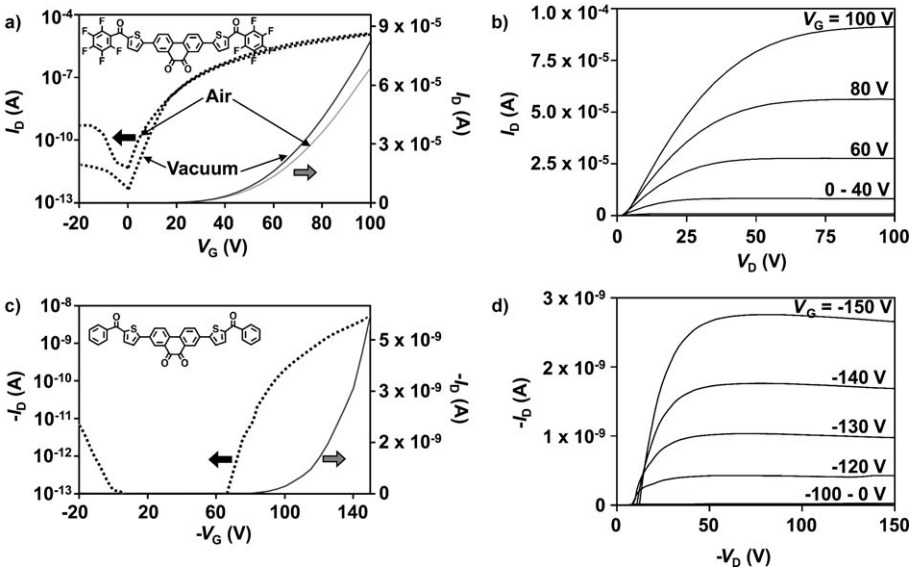

Figure 10. FET transfer (a, c) and output (b, d) plots measured under vacuum (and after 1 year in air for a) of vacuum deposited films of **5** (T_D = 150 °C) and **6** (T_D = 150 °C), respectively.

Oligomer and polymer film microstructure was adjusted to optimize device performance by varying the substrate temperature (T_D) during vacuum deposition and drop-casting. Solution-cast films of **1**–**4** were additionally annealed at 75 °C, 150 °C, and 250 °C with negligible effect on FET response. However, the performance of vapor-deposited **1** films is enhanced significantly as T_D increases (Table 4), from 25 °C (μ_e = 0.18 cm^{2}V^{-1}s^{-1}, $I_{on:off}$ = 3×10^5, V_T = +68 V), to a maximum at T_D = 80 °C (μ_e = 0.45 cm^{2}V^{-1}s^{-1}, $I_{on:off}$ = 1×10^8, V_T = +35 V). Under the optimized conditions, **1** exhibits low contact resistance and excellent saturation behavior in the output plots (Figure 9b), but does not exhibit FET activity under air. The FET performance of **2** also increases with T_D, from μ_h = 0.012 cm^{2}V^{-1}s^{-1} at 25 °C ($I_{on:off}$ = 10^5, V_T = −33 V), to a maximum μ_h of 0.043 cm^{2}V^{-1}s^{-1} at T_D = 90 °C ($I_{on:off}$ = 10^6, V_T = −19 V). Films of **2** exhibit ideal saturation behavior with only slight contact resistance (Figure 9d) and completely air-stable operation.

Solution-cast films of **1** and **2** exhibit impressive FET performance (Figure S2). The average μ_e for drop-cast **1** films is 0.21(8) cm^{2}V^{-1}s^{-1} (0.27 cm^{2}V^{-1}s^{-1} maximum) with a $I_{on:off}$ = 4×10^5, figures-of-merit similar to the vapor-deposited films. Drop-cast films of **2** exhibit an average μ_h of 8(4)×10^{-4} cm^{2}V^{-1}s^{-1} with $I_{on:off}$ = ≈10^4. Spin-cast and drop-cast films of polymer **3** exhibit a mobility of 1.7(6)×10^{-6} with an $I_{on:off}$ of 2(1)×10^2 and V_T = +52(10) V (Figure S2b). Blends of **1** and **3** were drop-cast to enhance FET performance while maintaining the favorable solution rheology of the polymer (500 ppm concentration at a 1:1 wt. ratio from xylenes), resulting in films exhibiting μ_e = 0.02(1) cm^{2}V^{-1}s^{-1} with $I_{on:off}$ = 3×10^4 and V_T = +68 V (Figure S2c).

Films of semiconductors **5** and **6** were vacuum-deposited at T_Ds ranging from 25 °C to 150 °C. Material **5** exhibits n-channel FET activity with performance increasing with T_D from μ_e = 5.3(2)×10^{-3} cm^{2}V^{-1}s^{-1} ($I_{on:off}$ = 8×10^5, V_T = +33(8) V) at 25 °C to μ_e = 0.017(2) cm^{2}V^{-1}s^{-1} ($I_{on:off}$ = 2×10^8, V_T = +28 (8) V) at 150 °C (Figure 10 and Table 5). The air stability of **5**-based n-channel FETs was evaluated over a period of 3 months (Figure 10a), revealing stable performance of μ_e = 0.015(3) cm^{2}V^{-1}s^{-1} ($I_{on:off}$ = 1×10^6, V_T = +26(5) V) after the initial device break-in (the performance of T_D = 150 °C devices was unchanged after >1 year in air). The output plot for **5**-based devices in Figure 10b reveals negligible contact resistance and excellent saturation behavior. Oligomer **6** also exhibits n-channel FET activity for T_D > 90 °C (Figure 10c,d and Table 5).

The performance increases slightly with T_D to a maximum μ_e = 1.2(2)×10^{-5} cm^{2}V^{-1}s^{-1} ($I_{on:off}$ = 2×10^4, V_T = +94(13) V)

Table 4. FET performance of vacuum-deposited semiconductor **1** and **2** films as a function of deposition temperature, measured under vacuum. Standard deviations are given in parentheses.

T_D [°C]	Semiconductor **1**			Semiconductor **2**		
	μ_e [$cm^2V^{-1}s^{-1}$]	V_T [V]	$I_{on:off}$	μ_h [$cm^2V^{-1}s^{-1}$]	V_T [V]	$I_{on:off}$
25	0.18(3)	68(12)	$3(1)\times10^5$	$1.2(3)\times10^{-2}$	−33(9)	$2(1)\times10^5$
50	0.17(2)	47(9)	$3(2)\times10^5$	$1.4(5)\times10^{-2}$	−27(4)	$5(2)\times10^5$
70	0.31(3)	45(7)	$8(2)\times10^5$	$2.8(8)\times10^{-2}$	−22(5)	$7(2)\times10^5$
80	0.45(5)	35(5)	$1(1)\times10^8$	$3.9(4)\times10^{-2}$	−17(3)	$2(2)\times10^6$
90	0.17(5)	34(4)	$2(1)\times10^7$	$4.3(7)\times10^{-2}$	−19(5)	$3(1)\times10^6$
Soln. Cast	0.21(8)	66(4)	$4(3)\times10^5$	$0.8(4)\times10^{-3}$	−32(6)	$5(3)\times10^3$

Table 5. FET performance of vacuum-deposited **5** and **6** films measured under vacuum. Standard deviations are given in parentheses.

T_D [°C]	Semiconductor **5**			Semiconductor **6**		
	μ_e [$cm^2V^{-1}s^{-1}$]	V_T [V]	$I_{on:off}$	μ_e [$cm^2V^{-1}s^{-1}$]	V_T [V]	$I_{on:off}$
25	$5.3(2)\times10^{-3}$	33(8)	$8(2)\times10^5$	–	–	–
50	$9.0(4)\times10^{-3}$	34(6)	$6(1)\times10^6$	–	–	–
90	$1.2(2)\times10^{-2}$	31(6)	$1(1)\times10^7$	$7.9(3)\times10^{-6}$	120(18)	$1(1)\times10^3$
120	$1.8(4)\times10^{-2}$	32(5)	$8(2)\times10^7$	$8.7(5)\times10^{-6}$	112(22)	$4(2)\times10^3$
150	$1.7(2)\times10^{-2}$	28(8)	$2(1)\times10^8$	$1.2(2)\times10^{-5}$	94(13)	$2(1)\times10^4$

at 150 °C. The output plot of **6** films reveals excellent saturation behavior and only slight contact resistance. Owing to the very-high sublimation temperatures of **5** and **6**, the chemical composition of the evaporation source and the resulting thin films was confirmed after film growth by H^1 NMR and elemental analysis, and was found to be consistent with the pure oligomers.

Crystal structures and solid-state packing: The structures of oligomers **1** and **2** as well as model compound **7** were determined by X-ray diffraction of single crystals grown by slow sublimation. Crystallographic experimental details and derived metrical parameters are summarized in Tables S1–S4 in the Supporting Information. Perfluorophenacyl oligomer **1** crystallizes in a monoclinic cell with a *C2/c* space group (Figure 11a,c). Unit cell dimensions are $a=53.617(12)$, $b=7.4030(17)$, $c=6.5735(15)$ Å, and $\beta=94.259(4)°$, giving a volume of 2602.0(10) $Å^3$. The quaterthiophene cores orient in a typical herringbone packing motif at an angle of 33°, with a π–π stacking distance of 3.50 Å (C14–C15′), and a maximum inter-thiophene torsion angle of 4°. The ancillary pentafluorophenyl groups are twisted with respect to the thiophene π-core at an angle of 53° and the carbonyl makes a 6° dihedral angle with the adjacent thiophene subunit. A single molecular layer is 26.77 Å thick with the pentafluorophenyl rings not interdigitated, but closely π-stacked (≈3.5 Å). Note that the packing of **1** is considerably different than previously observed for planar perfluoroarene-thiophene oligomers for which the electron-rich thiophene moiety overlaps with the electron-poor perfluoroarene, resulting in a face-to-face brick-like stacking and far shorter intermolecular stacking distances (<3.4 Å).[44] The present results reflect the large twist angle between flat quaterthiophene core and the pentafluorophenycl groups. Phenacyl oligomer **2** crystallizes in a monoclinic cell with a *P21/n* space group (Figure 11b,d). The unit cell dimensions are $a=6.0174(8)$, $b=7.4293(10)$, $c=52.685(7)$ Å, $\beta=93.137(2)°$, and the volume is 2351.8(5) $Å^3$. The quaterthiophene π-cores of **2** are also packed in a herringbone motif at a slightly decreased 26.5° angle, with the π–π stacking distance being 3.43 Å (C14–C16′) and a larger maximum inter-thiophene torsion of 13°. The phenyl groups are also twisted with respect to the thiophene π-core at an angle of 49°, but are not closely π-stacked as in **1**. The carbonyl axis lies 17° out of the plane of the adjacent thiophene subunit.

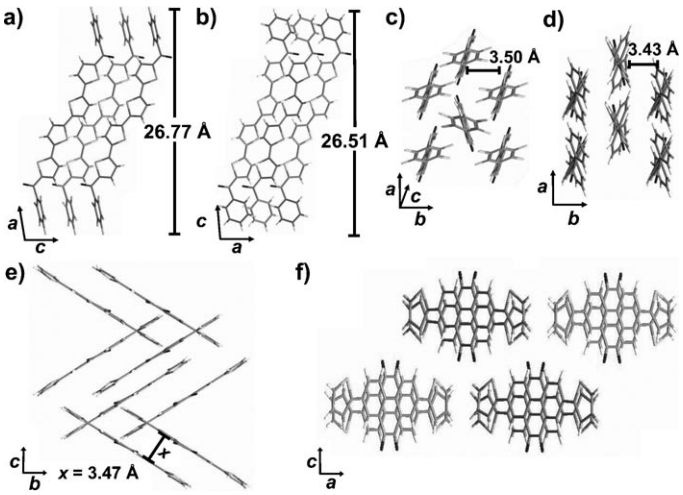

Figure 11. Crystal structures of semiconductors **1**, **2**, and **7**. Structures **1** and **2** are viewed along the cell *b* axes (a and b, respectively) and along the *c* axes (c and d, respectively). The crystal structure of **7** is viewed along the *a* axis (e) and *b* axis (f).

A single molecular layer is 26.51 Å thick with the phenyl rings not interdigitated. Quinone-based oligomer **7** crystallizes in an orthorhombic cell having the *Pbca* space group (Figure 11e,f). Unit cell dimensions are $a=12.5516(9)$, $b=12.9708(9)$, and $c=20.2613(14)$ Å, giving a volume of 3298.63(14) $Å^3$. The phenanthrenequinone core exhibits a slight 4.7° (C9–C8:C12–C13) torsion angle with the carbonyl carbons rotated slightly out of the anthracene plane and the connected thiophenes tilted at only 8.4° relative the phenanthrenequinone core. The molecules are π-stacked with the quinones aligned anti-parallel in a cofacial orientation at a close π–π distance of 3.47 Å (S2–C9). These π-stacks align

along the *b* axis and make an acute angle of 64.3° relative to each other (Figure 11e). A donor-acceptor packing motif is observed in **7**, with the molecules slipped 5.7 Å along the long axis of the molecule, overlapping the electron-deficient quinone with the electron-rich thiophene fragment.

Quantum chemical modeling: The molecular orbital (MO) energies and contours were calculated by using the DFT-optimized structures of molecules **1**, **2**, **5**, **6**, and **7** (Figure 12).

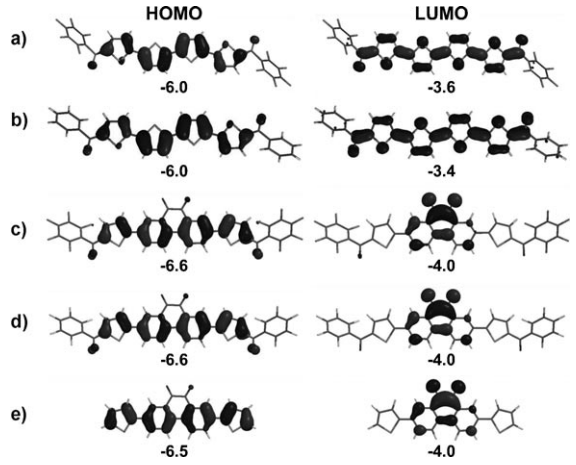

Figure 12. Molecular orbital electron density contour plots for oligomers a) **1**, b) **2**, c) **5**, d) **6**, and e) **7** viewed normal to the π-conjugated cores.

The computed π-conjugated quaterthiophene cores of **1** and **2** in the gas phase exhibit minimal intra-tetramer ring torsion, however the phenyl rings are twisted at 53 and 44°, respectively, from each quaterthiophene mean plane. The MO electron density plots reveal that the HOMO and LUMO are completely delocalized across the quaterthiophene core and carbonyl groups, with minimal phenyl substituent contribution. The computed HOMO energy for both **1** and **2** is −6.0 eV, whereas the LUMO energies are −3.6 and −3.4 eV, respectively. For molecules **5**–**7**, there is $<5°$ computed thiophene-phenanthrenequinone torsion angle, and the phenyl rings are twisted with respect to the π-core in **5** and **6**. The MO contours reveal that the HOMO is delocalized across the phenanthrenequinone and thiophene subunits. Interestingly, the LUMOs in **5**–**7** are localized on the phenanthrenequinone subunits (Figures 12c–e). The computed HOMO energies are −6.6, −6.6, and −6.5 V for **5**, **6**, and **7**, respectively, while the LUMO energies are all −4.0 eV for **5**–**7**.

Discussion

The correlations between organic semiconductor thin film morphology and FET performance will first be discussed in the context of the SEM, WAXRD, and FET data. Detailed molecular-level analysis will follow to examine the effect of molecular modifications and to interpret the observed FET device response. This analysis will utilize data from the single crystal X-ray structures, thermal analysis, optical spectroscopy, electrochemistry, and DFT-level MO analysis.

The FET device performance of each material was optimized by varying T_D for vapor-deposited and the annealing temperature drop-cast films. Spin-cast films optimized by varying the solvent and solvent mixtures were also investigated. A wide range of FET device responses and film microstructures were observed as a consequence of the film growth optimization studies. Materials **1**, **3**, **5**, and **6** are all found to exhibit n-channel FET activity under high-vacuum, and **5** also exhibits air-stable operation over a period greater than one year. Oligomer **2** exhibits p-channel behavior under high-vacuum and air, whereas no FET current modulation was observed in this study for films of model compounds **4** and **7**.

Thin-film microstructure and field-effect transistor device optimization: Top-contact bottom-gate FETs fabricated with vapor-deposited films of semiconductors **1**, **2**, **5**, and **6** were initially measured under vacuum. The performance of **1**-based devices increases with increasing T_D (Figures 9a,b and Figure 13a), from $\mu_e = 0.18(3)\ cm^2V^{-1}s^{-1}$ ($V_T = 68(12)$ V, $I_{on:off} = 3(1)\times10^5$) at $T_D = 25\,°C$ to $\mu_e = 0.45(5)\ cm^2V^{-1}s^{-1}$ ($V_T = 35(5)$ V, $I_{on:off} = 1(1)\times10^8$) at $T_D = 80\,°C$, before diminishing slightly at $T_D = 90\,°C$ (Table 4). This performance enhancement corresponds to an increase in crystallite grain size observed in SEM images from ≈100 nm at $T_D = 25\,°C$ to > 1 μm at $T_D = 90\,°C$ (Figures 7a–c). WAXRD data for the films indicate that the overall crystallinity also increases with T_D, although reflections from a second phase begin to appear at 90 °C (Figure 6a). Such a phase-impurity can diminish μ, as observed in this study, by creating defect sites

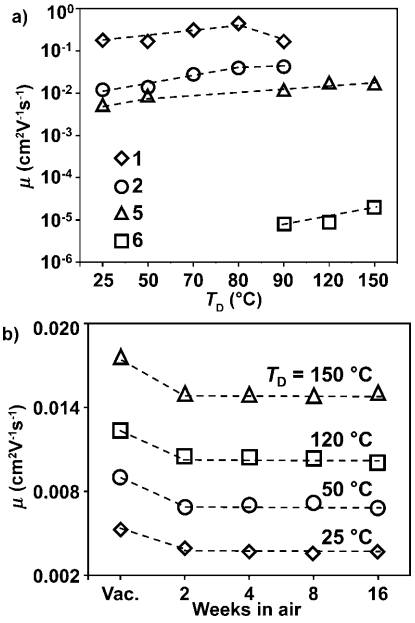

Figure 13. Plot of measured FET μ vs. T_D for oligomers **1**, **2**, **5**, and **6** (a) and μ vs. number of weeks storage in air for **5** films deposited at the indicated T_D (b). Dashed lines are a guide for the eye.

in the film that scatter or trap charge carriers.[15,41] The *d*-spacing of the dominant phase, 26.6 ± 0.1 Å, corresponds well with the height of one molecular layer determined from the single-crystal structure determination, 26.77 Å, indicating that the long axis of the molecule is aligned along the substrate normal.

Non-fluorinated phenacyl molecule **2** exhibits p-channel FET behavior that also improves with T_D (Figures 9c,d and Figure 13a) from $\mu_h = 0.012(3)\ cm^2V^{-1}s^{-1}$ ($V_T = -33(9)$ V, $I_{on:off} = 2(1)\times10^5$) at $T_D = 25\,°C$ to $\mu_h = 0.043(7)\ cm^2V^{-1}s^{-1}$ ($V_T = -19(5)$ V, $I_{on:off} = 3(1)\times10^6$) at $T_D = 90\,°C$ (Table 4). FET performance is unchanged when measured in air. As with the fluorinated analog **1**, this performance enhancement coincides with an increase in average crystallite size observed in SEM images of **2**-derived films from ≈100 nm at $T_D = 25\,°C$ to ≈1 μm at $T_D = 90\,°C$ (Figures 7d–f). The WAXRD reflection intensity from **2**-derived films also increases with increasing T_D, indicating that the overall film crystallinity is enhanced (Figure 8). The 26.31 ± 0.1 Å *d*-spacing calculated from the Bragg progression corresponds well with the height of one molecular layer determined from the single-crystal structure determination, 26.51 Å, indicating that the long axis of the molecule is aligned parallel to the substrate normal.

Quinone-containing oligomer **5** exhibits n-channel FET behavior when measured both in vacuum and under air (Figure 10a, b and Figure 13). The FET performance improves with increasing T_D when measured under vacuum from $\mu_e = 5.3(2)\times10^{-3}\ cm^2V^{-1}s^{-1}$ ($V_T = 33(8)$ V, $I_{on:off} = 8(2)\times10^5$) at $T_D = 25\,°C$ to $\mu_e = 0.018(4)\ cm^2V^{-1}s^{-1}$ ($V_T = 28(8)$ V, $I_{on:off} = 2(1)\times10^8$) at $T_D = 150\,°C$ (Table 5). When measured in air, V_T exhibits negligible change and μ_e exhibits a slight decrease in magnitude to $0.015(3)\ cm^2V^{-1}s^{-1}$ ($V_T = 31(12)$ V, $I_{on:off} = 5(1)\times10^6$) at $T_D = 150\,°C$ (Figure 13b), which is stable for greater than one year when stored and measured under laboratory air. The WAXRD data indicate phase-pure films having a *d*-spacing of 27.9 ± 0.1 Å, which corresponds closely with the 28.0 Å height of one molecular layer (determined from the DFT geometry plus a 0.3 Å interlayer spacing adjustment, estimated from that observed in the crystal structure of **1**). This indicates that the long axis of the molecule is aligned normal to the substrate surface, a motif similar to that of **1** and **2**.

Oligomer **6** also exhibits n-channel FET activity under vacuum for $T_D > 90\,°C$ (Figure 10c,d and Figure 13a). Performance improves with increasing T_D from $\mu_e = 7.9(3)\times10^{-6}\ cm^2V^{-1}s^{-1}$ ($V_T = 120(18)$ V, $I_{on:off} = 1(1)\times10^3$) at $T_D = 90\,°C$ to $\mu_e = 1.2(2)\times10^{-5}\ cm^2V^{-1}s^{-1}$ ($V_T = 94(13)$ V, $I_{on:off} = 2(1)\times10^4$) at $T_D = 150\,°C$ (Table 5). This diminished μ_e relative to the other vapor-deposited oligomers **1**, **2**, and **5** is likely attributable to a different thin-film crystal phase that is revealed by the WAXRD data. Note that no decomposition is observed upon sublimation of **6**. Also, the experimental and DFT-computed frontier MO energies reveal that **5** and **6** are isoenergetic and isogeometric (Table 2 and Figure 12), so the difference in FET performance is not intrinsically MO-based. The dominant family of Bragg reflections corresponds to a *d*-spacing of 25.90 ± 0.08 Å, arguing that the molecules are tilted at ≈69.0° relative to the substrate surface (calculated using the DFT optimized geometry plus a 0.3 Å interlayer spacing adjustment). This tilt angle is similar to the 64.3° mutual angle made by the slipped dimers in the single-crystal X-ray diffraction derived structure of **7** (Figure 11). Such a slipped structure can potentially decrease the efficiency of π–π charge transport compared to completely overlapped/eclipsed oligomers such as in the crystal structures of **1**, **2**, and **5**. There is a second, minority phase observed in **6** films grown at $T_D = 150\,°C$ with a 27.05 ± 0.04 Å *d*-spacing, which suggests a more upright molecular orientation. Although this second phase may exhibit stronger intermolecular π–π coupling, the dominant, tilted phase likely limits FET performance. The SEM images of **6** films also reveal a morphology substantially different from the other oligomers, with a more homogenous surface that begins to exhibit void spaces of ≈1 μm dimensions at $T_D = 150\,°C$. Model compound **7** does not exhibit FET activity or show evidence of thin-film crystallinity under the present growth conditions.

Materials **1**–**3** afford uniform films when drop-cast from common organic solvents, while spin-casting of **3** also yields highly uniform films. Drop-cast films of oligomers **1** and **2** exhibit outstanding FET response (Figure S2a) with $\mu_e = 0.21(8)\ cm^2V^{-1}s^{-1}$ ($V_T = 66(4)$ V, $I_{on:off} = 4\ (3)\times10^5$) and $\mu_h = 8\ (4)\times10^{-4}\ cm^2V^{-1}s^{-1}$ ($V_T = -32(6)$ V, $I_{on:off} = 5\ (30)\times10^3$), respectively. The FET performance of **1** is one of the most impressive reported to date for a solution-cast organic semiconductor. Indeed, films of both materials are highly crystalline and exhibit the same XRD pattern as the vapor-deposited films (Figure 6). Furthermore, SEM images and optical microscopy of drop-cast films of **1** reveal very large crystalline plates with dimensions up to 0.1 mm (Figure 7g and Figure S1a, respectively) which are even larger than what observed for vapor-deposited **1** films.

Drop-cast and spin-cast films of polymer **3** exhibit a mobility of $1.7(6)\times10^{-6}$. Although **1** and **2** films exhibit very intense Bragg reflections, **3** films do not, indicating poor film crystallinity that may impede carrier mobility. To enhance the film FET performance while maintaining favorable solution rheology, solutions of oligomer **1** and polymer **3** were blended. An equal wt.: wt. ratio of molecule : polymer yields films exhibiting $\mu_e = 0.02(1)\ cm^2V^{-1}s^{-1}$ with $I_{on:off} = 3\times10^4$ and $V_T = +68$ V. This unique polymer-oligomer blend solution combines the favorable rheological characteristics of the polymer solution with the high FET performance of molecule **1** to yield a more processable solution, affording excellent semiconductor films for FETs. Molecule **4** was designed to assess whether repositioning the *n*-alkyl solubilizing groups from the inner two thiophenes of the quaterthiophene core in **3** to the outer thiophenes would result in higher crystallinity and therefore enhanced FET performance. However, films of **4** either vacuum-deposited or drop-cast do not exhibit Bragg reflections, indicating that the substituent repositioning does not enhance thin-film crystallinity.

Electronic properties, molecular modeling, and crystal packing: Although a thin-film microstructure can significantly impact FET device response, the intrinsic molecular properties of an organic semiconductor ultimately determine the performance limits.[53–55] The primary molecular-level considerations are crystal packing and frontier orbital delocalization/energetics/overlap. In this study, optical spectroscopy, single crystal X-ray structure determination, electrochemistry, and DFT-level computational modeling are employed to probe these properties experimentally and theoretically.

Since charge is transported through the frontier molecular orbitals of organic semiconductors, their geometries, energies, and extents of delocalization directly affect carrier stability and intermolecular hopping rates. Ideally, the HOMO and LUMO are delocalized over the entire π-core of the semiconductor for p- and n-channel transport, respectively.[41,56] Delocalization, such as that observed in the DFT-derived MO contour plots of **1** and **2**, enhances the charge transfer rate by increasing charge stabilization and intermolecular π-overlap while minimizing Marcus reorganization energies.[41,45] (Figures 12a,b). Interestingly, although the HOMOs of **5**–**7** are well delocalized, the LUMOs are localized on the phenanthrenequinone subunits (Figure 12c–e). This highly localized nature of the LUMO reduces π-overlap compared to the ideal delocalization present in **1** and **2** and may favor electron trapping at the quinone site. This localization may be a contributing factor to the the diminished μ_e values of compounds **5** and **6** compared to **1**, despite the greater electron affinity.

The MO energies affect charge carrier stability and are a key parameter in rationalizing the charge carrier signs in standard OFET devices. In materials **1**–**4**, the phenacyl ancillary substituents stabilize the LUMO, diminishing the susceptibility of the mobile electrons to trapping (Table 2).[13,41,42,57] In the case of **1** and **3**, this stabilization lowers the LUMOs to −3.6 and −3.4 eV, respectively, sufficient to enable n-channel activity on HMDS-treated SiO_2. Indeed, these energies are below the threshold postulated for efficient n-channel activity in the presence of surface hydroxyl groups,[15,58,59] but probably insufficient for n-channel activity in the presence of air-based trapping species.[16,37]

Quinone moieties were introduced into the π-core here to further stabilize the LUMO and enable air-stable n-channel FET operation. Previous reports on NDI-F[16,29] and $CuF_{16}Pc$[27,30–32] proposed that LUMO energies below −3.9 eV are sufficient to enable air-stable n-channel FET operation for perfluoroalkyl-substituted semiconductors. The present computational modeling reveals that introduction of either bithiophene-quinone (**21**), phenanthrenequinone, or pyrene-4,5,9,10-tetraone (**24**) fragments can displace the LUMO energy below this −3.9 eV threshold. Although all of the proposed quinone-containing cores (**21**, **22**, **24**) were successfully synthesized in this work, only the Suzuki coupling reactions involving 2,7-diiodo-9,10-phenanthrenequinone (**22**) were productive, yielding materials **5**–**7**.

As predicted, the fluorinated oligomer **5** exhibits air-stable n-channel operation, while the non-fluorinated analog **6** does not. The ambient stability of **5** is likely the result of the more tightly packed perfluorophenyl versus phenyl ancillary substituents since the LUMO energies of **5** (−4.03 eV) and **6** (−4.02 eV) as well as their geometries are similar. This result is in agreement with previous studies suggesting that fluorocarbon substitution of a semiconductor with a LUMO energy below −3.9 eV creates an O_2-barrier, preventing O_2 from trapping mobile electrons in the FET channel.[16] Additionally, semiconductor **5** maintains a high $I_{on:off}$ ratio of 10^6 since the LUMO energy (−4.03 eV) is above the −4.2 eV level at which ambient doping has previously been observed in extremely-high electron-affinity organic semiconductors.[26,37]

The crystal packing motifs of **1** and **2** are similar, with the quaterthiophene cores herringbone-packed at distances of 3.50 and 3.43 Å, respectively (Figure 11). This type of herringbone π-stacking motif has been shown experimentally and theoretically to afford optimal π-overlap in quaterthiophene-based semiconductors.[44,60] The structure of both materials reveals two layers of π-stacked molecules per unit cell, with the out-of-plane phenyl substituents locking the π-stacked molecules into an orientation normal to the *ac* plane. In polymer **3**, introduction of the n-octyl solubilizing group, in combination with the phenyl-thiophene dihedral angle along the polymer backbone, likely disrupts the herringbone π-stacked layers, resulting in the observed decreased thin-film crystallinity and poorer FET performance. Model compound **4** was synthesized to evaluate how crystallinity is affected when the alkyl substituents are moved toward the edge of the π-core. The crystal lattice is also destabilized with the groups in this location, resulting in **4** being extremely-soluble but producing amorphous films.

The X-ray diffraction-derived structure of quinone model compound **7** reveals a highly-planar π-core architecture with molecules cofacially π-stacked (Figure 11e, f). Stacked molecules are slipped ≈5.7 Å along the long axis of the molecule and make a 64° angle from one π-stack with respect to the next, likely induced by a donor-acceptor interaction of the electron-rich thiophene fragment with the electron-deficient quinone subunit. The quinones also stack antiparallel owing to stabilizing dipole–dipole interactions. This slipped structure, which diminishes intermolecular π–π coupling, is likely similar to the dominant phase of **6** films, where the molecules are tilted ≈69° relative to the substrate surface. This structure of **7** provides evidence for the high crystal packing affinity of quinine-containing materials and also insight into the diminished mobility of **6**-derived films.

Conclusions

The present family of phenacyl–thiophene and quinine-based semiconductors exhibits rich and informative relationships between molecular-level electronic/structural properties, film processability, thin-film morphology, and p-/n-channel FET device characteristics. The design strategy to concurrently enhance solubility and crystal packing yields high-

performance solution processable n-channel FET materials with μ_e up to $\approx 0.3\,cm^2V^{-1}s^{-1}$ for solution-cast films of **1** and one of the first n-channel polymers prepared to date (**3**). Blending **1** with **3** enhances both solution rheology and FET device performance from $\mu_e \approx 10^{-6}\,cm^2V^{-1}s^{-1}$ for neat **3** films to $\approx 0.02\,cm^2V^{-1}s^{-1}$ for blend films. A computational study of LUMO stabilization reveals that introduction of quinone units into the π-conjugated core enables air-stable n-channel operation. Introduction of a phenanthrenequinone unit, one of the three quinones identified, affords oligomer **5**, also exhibiting air-stable n-channel FET operation with $\mu_e \approx 0.02\,cm^2V^{-1}s^{-1}$ and a high $I_{on:off} = 10^6$ under ambient conditions. The non-fluorinated phenanthrenequinone analog **6** exhibits diminished $\mu_e \approx 10^{-5}\,cm^2V^{-1}s^{-1}$ and air-unstable FET operation, in agreement with the O_2-barrier model proposed previously. Films of **6** also exhibit a different thin-film phase from that of the other oligomers, likely with diminished intermolecular π–π coupling and likely responsible for the depressed μ_e. The crystal structures of quaterthiophene compounds **1** and **2** reveal that both pack in a herringbone motif with short π-stacking distances and a layered structure. The first crystal structure of a quinone-containing thiophene-based molecule **7** reveals anti-parallel dipole alignment and cofacial packing with a short 3.48 Å π–π stacking distance. This work demonstrates that rational design can yield extremely π-electron-deficient monomer units for use in air-stable n-channel FET molecular and polymer semiconductors.

Acknowledgements

We thank the Northwestern MRSEC (NSF-MRSEC DMR-0520513) and AFOSR (FA9550-08-1-0331 for support of this research. R.P.O. acknowledges the MICINN of Spain for a personal postdoctoral grant.

[1] a) S.-H. Hwang, C. N. Moorefield, G. R. Newkome, *Chem. Soc. Rev.* **2008**, *37*, 2543; b) J. Meyer, T. Winkler, S. Hamwi, S. Schmale, H.-H. Johannes, T. Weimann, P. Hinze, W. Kowlasky, T. Riedl, *Adv. Mater.* **2008**, *20*, 3839; c) G. H. Gelinck, H. E. A. Huitema, E. Van Veenendaal, E. Cantatore, L. Schrijnemakers, J. Van der Putten, T. C. T. Geuns, M. Beenhakkers, J. B. Giesbers, B. H. Huisman, E. J. Meijer, E. M. Benito, F. J. Touwslager, A. W. Marsman, B. J. E. Van Rens, D. M. De Leeuw, *Nat. Mater.* **2004**, *3*, 106; d) L. S. Hung, C. H. Chen, *Mat. Sci. Eng. R* **2002**, *39*, 143; e) O. Prache, *Displays* **2001**, *22*, 49.

[2] a) M. C. Gather, F. Ventsch, K. Meerholz, *Adv. Mater.* **2008**, *20*, 1966; b) M. E. Roberts, S. C. B. Mannsfeld, N. Queralto, C. Reese, J. Locklin, W. Knoll, Z. Bao, *Proc. Natl. Acad. Sci. USA* **2008**, *105*, 12134; c) L. Torsi, G. M. Farinola, F. Marinelli, M. C. Tanese, O. H. Omar, L. Valli, F. Babudri, F. Palmisano, P. G. Zambonin, F. Naso, *Nat. Mater.* **2008**, *7*, 412; d) D. A. Bernards, D. J. Macaya, M. Nikolou, J. A. DeFranco, S. Takamatsu, G. G. Malliaras, *J. Mater. Chem.* **2008**, *18*, 116; e) Y. T. Jeong, B. H. Cobb, S. D. Lewis, A. Dodabalapur, S. Lu, A. Facchetti, T. J. Marks, *Appl. Phys. Lett.* **2008**, *93*, 133304/1; f) Y.-Y. Noh, D.-Y. Kim, *Solid-State Electron.* **2007**, *51*, 1052; g) I. Manunza, A. Bonfiglio, *Biosens. Bioelectron.* **2007**, *22*, 2775; h) Q. Zhang, V. Subramanian, *Biosens. Bioelectron.* **2007**, *22*, 3182; i) D. J. Macaya, M. Nikolou, S. Takamatsu, J. T. Mabeck, R. M. Owens, G. G. Malliaras, *Sens. Actuators B* **2007**, *123*, 374.

[3] a) C. J. Brabec, J. R. Durrant, *MRS Bull.* **2008**, *33*, 670; b) B. C. Thompson, J. M. J. Frechet, *Angew. Chem.* **2008**, *120*, 62; *Angew. Chem. Int. Ed.* **2008**, *47*, 58; c) C. Yang, J. Y. Kim, S. Cho, J. K. Lee, A. J. Heeger, F. Wudl, *J. Am. Chem. Soc.* **2008**, *130*, 6444; d) M. T. Lloyd, J. E. Anthony, G. G. Malliaras, *Mater. Today* **2007**, *10*, 34; e) J. Roncali, P. Leriche, A. Cravino, *Adv. Mater.* **2007**, *19*, 2045; f) N. Koch, *ChemPhysChem* **2007**, *8*, 1438; g) H. Spanggaard, F. C. Krebs, *Sol. Energy Mater.* **2004**, *83*, 125.

[4] a) Q. Tang, L. Jiang, Y. Tong, H. Li, Y. Liu, Z. Wang, W. Hu, Y. Liu, D. Zhu, *Adv. Mater.* **2008**, *20*, 2947; b) H. Yamada, T. Okujima, N. Ono, *Chem. Commun.* **2008**, 2957; c) B. S. Ong, Y. Wu, Y. Li, P. Liu, H. Pan, *Chem. Eur. J.* **2008**, *14*, 4766; d) S. Allard, M. Forster, B. Souharce, H. Thiem, U. Scherf, *Angew. Chem.* **2008**, *120*, 4138; *Angew. Chem. Int. Ed.* **2008**, *47*, 4070; e) *Organic Electronics* (Ed.: H. Klauk), Wiley-VCH, Weinheim, **2006**, p. 428; f) G. H. Gelinck, H. E. A. Huitema, E. Van Veenendaal, E. Cantatore, L. Schrijnemakers, J. Van der Putten, T. C. T. Geuns, M. Beenhakkers, J. B. Giesbers, B. H. Huisman, E. J. Meijer, E. M. Benito, F. J. Touwslager, A. W. Marsman, B. J. E. Van Rens, D. M. De Leeuw, *Nat. Mater.* **2004**, *3*, 106; g) T. W. Kelley, P. F. Baude, C. Gerlach, D. E. Ender, D. Muyres, M. A. Haase, D. E. Vogel, S. D. Theiss, *Chem. Mater.* **2004**, *16*, 4413; h) R. J. Chesterfield, J. C. McKeen, C. R. Newman, P. C. Ewbank, D. A. da Silva, J. L. Bredas, L. L. Miller, K. R. Mann, C. D. Frisbie, *J. Phys. Chem. B* **2004**, *108*, 19281; i) C. D. Dimitrakopoulos, R. L. Malefant, *Adv. Mater.* **2002**, *14*, 99; j) *Printed Organic and Molecular Electronics*, (Eds.: D. R. Gamota, P. Brazis, K. Kalyanasundaram, J. Zhang), Springer, Stuttgart, **2004**, p. 720; k) W. Fix, A. Ullmann, J. Ficker, W. Clemens, *Appl. Phys. Lett.* **2002**, *81*, 1735; l) G. H. Gelinck, T. C. T. Geuns, D. M. de Leeuw, *Appl. Phys. Lett.* **2000**, *77*, 1487; m) *Handbook of Oligo- and Polythiophenes* (Ed.: D. Fichou), Wiley-VCH, Weinheim, **1999**; n) T. A. Skotheim, R. L. Elsenbaumer, J. R. Reynolds, *Handbook of Conductive Polymers*, Marcel Dekker, New York, **1998**; o) T. A. Skotheim, R. L. Elsenbaumer, J. R. Reynolds, *Handbook of Conductive Polymers*, Marcel Dekker, New York, **1998**.

[5] a) X.-H. Zhang, B. Kippelen, *J. Appl. Phys.* **2008**, *104*, 104504/1; b) R. T. Weitz, K. Amsharov, U. Zschieschang, E. Barrena Villas, D. K. Goswami, M. Burghard, H. Dosch, M. Jansen, K. Kern, H. Klauk, *J. Am. Chem. Soc.* **2008**, *130*, 4637; c) H. Yan, Y. Zheng, R. Blache, C. Newman, S. Lu, J. Woerle, A. Facchetti, *Adv. Mater.* **2008**, *20*, 3393; d) H. E. Katz, *Semicond. Polym.* **2007**, *2*, 567; e) S. Handa, E. Miyazaki, K. Takimiya, Y. Kunugi, *J. Am. Chem. Soc.* **2007**, *129*, 11684; f) K. Kashiwagi, T. Yasuda, T. Tsutsui, *Chem. Lett.* **2007**, *36*, 1194; g) M. J. Panzer, C. D. Frisbie, *J. Am. Chem. Soc.* **2007**, *129*, 6599; h) S. Günes, H. Neugebauer, S. N. Serdar, *Chem. Rev.* **2007**, *107*, 1324; i) S. R. Amrutha, M. Jayakannan, *Macromolecules* **2007**, *40*, 2380; j) W. Ma, C. Yang, X. Gong, K. Lee, A. J. Heeger, *Adv. Funct. Mater.* **2005**, *15*, 1617; k) T. Kietzke, H. H. Horhold, D. Neher, *Chem. Mater.* **2005**, *17*, 6532; l) S. Scheinert, G. Paasch, *Phys. Status Solidi A* **2004**, *201*, 1263; m) B. S. Ong, Y. Wu, P. Liu, S. Gardner, *J. Am. Chem. Soc.* **2004**, *126*, 3378; n) S. E. Shaheen, C. J. Brabec, N. S. Sariciftci, F. Padinger, T. Fromherz, J. C. Hummelen, *Appl. Phys. Lett.* **2001**, *78*, 841.

[6] a) K. H. Kim, Z. Chi, M. J. Cho, J.-I. Jin, M. Y. Cho, S. J. Kim, J.-S. Joo, D. H. Choi, *Synth. Met.* **2007**, *157*, 497; b) T. B. Singh, S. Erten, S. Gunes, C. Zafer, G. Turkmen, B. Kuban, Y. Teoman, N. S. Sariciftci, S. Icli, *Org. Electron.* **2006**, *7*, 480.

[7] a) J. Chen, S. Subramanian, S. R. Parkin, M. Siegler, K. Gallup, C. Haughn, D. C. Martin, J. E. Anthony, *J. Mater. Chem.* **2008**, *18*, 1961; b) J. E. Anthony, *Chem. Rev.* **2006**, *106*, 5028.

[8] a) A. Afzali, C. R. Kagan, G. P. Traub, *Synth. Met.* **2005**, *155*, 490; b) D. M. DeLongchamp, S. Sambasivan, D. A. Fischer, E. K. Lin, P. Chang, A. R. Murphy, J. M. J. Frechet, V. Subramanian, *Adv. Mater.* **2005**, *17*, 2340; c) A. R. Murphy, J. M. J. Frechet, P. Chang, J. Lee, V. Subramanian, *J. Am. Chem. Soc.* **2004**, *126*, 1596; d) A. Afzali, C. D. Dimitrakopoulos, T. L. Breen, *J. Am. Chem. Soc.* **2002**, *124*, 8812; e) P. T. Herwig, K. Mullen, *Adv. Mater.* **1999**, *11*, 480; f) A. R. Brown, A. Pomp, D. M. de Leeuw, D. B. M. Klaassen, E. E. Havinga,

P. Herwig, K. Mullen, *J. Appl. Phys.* **1996**, *79*, 2136; g) A. R. Brown, A. Pomp, C. M. Hart, D. M. de Leeuw, *Science* **1995**, *270*, 972.
[9] A. Facchetti, *Mater Today* **2007**, *10*, 28.
[10] a) Y. D. Park, J. A. Lim, H. S. Lee, K. Cho, *Mater. Today* **2007**, *10*, 46; b) J. Locklin, M. Roberts, S. Mannsfeld, Z. Bao, *J. Macromol. Sci. Polym. Rev.* **2006**, *46*, 79; c) Y. Shao, S. A. Solin, D. R. Hines, E. D. Williams, *J. Appl. Phys.* **2006**, *100*, 044512/1; d) M. Surin, P. Leclerc, R. Lazzaroni, J. D. Yuen, G. Wang, D. Moses, A. J. Heeger, S. Cho, K. Lee, *J. Appl. Phys.* **2006**, *100*, 033712/1; e) A. L. Deman, J. Tardy, *Mater. Sci. Eng. C* **2006**, *26*, 421; f) H. S. Lee, D. H. Kim, J. H. Cho, Y. D. Park, J. S. Kim, K. Cho, *Adv. Funct. Mater.* **2006**, *16*, 1859.
[11] a) K. Tsukagoshi, K. Shigeto, I. Yagi, Y. Aoyagi, *Appl. Phys. Lett.* **2006**, *89*, 113507; b) A. Facchetti, M.-H. Yoon, T. J. Marks, *Adv. Mater.* **2005**, *17*, 1705; c) R. Schroeder, L. A. Majewski, M. Grell, *Adv. Mater.* **2005**, *17*, 1535; d) P. S. Abthagir, Y.-G. Ha, E.-A. You, S.-H. Jeong, H.-S. Seo, J.-H. Choi, *J. Phys. Chem. B* **2005**, *109*, 23918; e) D. M. DeLongchamp, S. Sambasivan, D. A. Fischer, E. K. Lin, P. Chang, A. R. Murphy, J. M. J. Frechet, V. Subramanian, *Adv. Mater.* **2005**, *17*, 2340; f) T. B. Singh, F. Meghdadi, S. Günes, N. Marjanovic, G. Horowitz, P. Lang, S. Bauer, N. S. Sariciftci, *Adv. Mater.* **2005**, *17*, 2315; g) T. Jung, A. Dodabalapur, R. Wenz, S. Mohapatra, *Appl. Phys. Lett.* **2005**, *87*, 182109.
[12] a) Y. Yang, K. Shin, C. E. Park, *Adv. Funct. Mater.* **2005**, *15*, 1806; b) K. P. Pernstich, S. Haas, D. Oberhoff, C. Goldmann, D. J. Gundlach, B. Batlogg, A. N. Rashid, G. J. Schitter, *J. Appl. Phys.* **2004**, *96*, 6431; c) S. Pratontep, M. Brinkmann, F. Nuesch, L. Zuppiroli, *Synth. Met.* **2004**, *146*, 387; d) P. V. Pesavento, R. J. Chesterfield, C. R. Newman, C. D. Frisbie, *J. Appl. Phys.* **2004**, *96*, 7312; e) J. Lee, J. H. Kim, S. Im, *J. Appl. Phys.* **2004**, *95*, 3733; f) A. Salleo, R. A. Street, *J. Appl. Phys.* **2003**, *94*, 471; g) D. Knipp, R. A. Street, A. Volkel, A. Ho, *J. Appl. Phys.* **2003**, *93*, 347; h) H. Klauk, M. Halik, U. Zschieschang, G. Schmid, W. Radlik, W. Weber, *J. Appl. Phys.* **2002**, *92*, 5259; i) M. L. Chabinyc, M. S. Yang, R. A. Street, *Appl. Phys. Lett.* **2002**, *81*, 4260.
[13] a) C. Kim, A. Facchetti, T. J. Marks, *Science* **2007**, *318*, 76; b) C. Kim, A. Facchetti, T. J. Marks, *Adv. Mater.* **2007**, *19*, 2561.
[14] a) T. Fujiwara, J. Locklin, Z. Bao, *Appl. Phys. Lett.* **2007**, *90*, 232108; b) T. D. Anthopoulos, F. B. Kooistra, H. J. Wondergem, D. Kronholm, J. C. Hummelen, D. M. de Leeuw, *Adv. Mater.* **2006**, *18*, 1679; c) I. O. Shklyarevskiy, P. Jonkheijm, N. Stutzmann, D. Wasserberg, H. J. Wondergem, P. C. M. Christianen, A. P. H. J. Schenning, D. M. De Leeuw, Z. Tomovic, J. Wu, K. Muellen, J. C. Maan, *J. Am. Chem. Soc.* **2005**, *127*, 16233; d) W. Pisula, A. Menon, M. Stepputat, I. Lieberwirth, U. Kolb, A. Tracz, H. Sirringhaus, T. Pakula, K. Muellen, *Adv. Mater.* **2005**, *17*, 684; e) N. Stingelin-Stutzmann, E. Smits, H. Wondergem, C. Tanase, P. Blom, P. Smith, D. de Leeuw, *Nat. Mater.* **2005**, *4*, 601; f) M. L. Swiggers, G. Xia, J. D. Slinker, A. A. Gorodetsky, G. G. Malliaras, R. L. Headrick, B. T. Weslowski, R. N. Shashidhar, C. S. Dulcey, *Appl. Phys. Lett.* **2001**, *79*, 1300; g) A. Tracz, J. K. Jeszka, M. D. Watson, W. Pisula, K. Muellen, T. Pakula, *J. Am. Chem. Soc.* **2003**, *125*, 1682; h) C. Liu, A. J. Bard, *Chem. Mater.* **2000**, *12*, 2353; i) X. L. Chen, Z. Bao, B. J. Sapjeta, A. J. Lovinger, B. Crone, *Adv. Mater.* **2000**, *12*, 344; j) K. C. Dickey, J. E. Anthony, Y. Loo, *Adv. Mater.* **2006**, *18*, 1721.
[15] H. A. Becerril, M. E. Roberts, Z. Liu, J. Locklin, Z. Bao, *Adv. Mater.* **2008**, *20*, 2588.
[16] G. S. Tulevski, Q. Miao, A. Afzali, T. O. Graham, C. R. Kagan, C. Nuckolls, *J. Am. Chem. Soc.* **2006**, *128*, 1788.
[17] D. J. Gundlach, J. E. Royer, S. K. Park, S. Subramanian, O. D. Jurchescu, B. H. Hamadani, A. J. Moad, R. J. Kline, L. C. Teague, O. Kirillov, C. A. Richter, J. G. Kushmerick, L. J. Richter, S. R. Parkin, T. N. Jackson, J. E. Anthony, *Nat. Mater.* **2008**, *7*, 216.
[18] A. Babel, S. A. Jenekhe, *J. Am. Chem. Soc.* **2003**, *125*, 13656.
[19] a) Z. Chen, Y. Zheng, H. Yan, A. Facchetti, *J. Am. Chem. Soc.* **2009**, *131*, 8; b) H. Yan, Z. Chen, Y. Zheng, C. E. Newman, J. Quin, F. Dolz, M. Kastler, A. Facchetti, *Nature* **2009**, *457*, 679; c) J. Letizia, M. Salata, C. Tribout, A. Facchetti, M. A. Ratner, T. J. Marks, *J. Am. Chem. Soc.* **2008**, *130*, 9679.
[20] a) R. Capelli, F. Dinelli, S. Toffanin, F. Todescato, M. Murgia, M. Muccini, A. Facchetti, T. J. Marks, *J. Phys. Chem. C* **2008**, *112*, 12993; b) J. Zaumseil, R. Friend, H. Sirringhaus, *Nat. Mater.* **2006**, *5*, 69; c) A. Facchetti, G. R. Dholakia, M. Meyyappan, T. J. Marks, *NanoLetters* **2006**, *6*, 2447; d) J. S. Swensen, C. Soci, A. Heeger, *Appl. Phys. Lett.* **2005**, *87*, 253511.
[21] a) J. Grimshaw, *Organic Electrochemistry: An Introduction and a Guide*, 4th ed., Dekker New York, **2000**, Chapter 10, p. 411; b) C.-I. Wu, G.-R. Lee, T.-W. Pi, *Appl. Phys. Lett.* **2005**, *87*, 212108; c) M. G. Mason, C. W. Tang, L. S. Hung, P. Raychaudhuri, J. Madathil, D. J. Giesen, L. Yan, Q. T. Le, Y. Gao, S. T. Lee, L. S. Liao, L. F. Cheng, W. R. Salaneck, D. A. dos Santos, J. L. Brédas, *J. Appl. Phys.* **2001**, *89*, 2756; d) C. Shen, A. Kahn, J. Schwartz, *J. Appl. Phys.* **2001**, *89*, 449; e) C. Cheng, A. Kahn, J. Schwartz, *J. Appl. Phys.* **2001**, *90*, 6536; f) Q. T. Le, L. Yan, Y. Gao, M. G. Mason, D. J. Giesen, C. W. Tang, *J. Appl. Phys.* **2000**, *87*, 375; g) Y. Hirose, A. Kahn, V. Aristov, P. Soukiassian, V. Bulovic, S. R. Forrest, *Phys. Rev. B* **1996**, *54*, 13748.
[22] C. R. Newman, C. D. Frisbie, D. A. da Silva Filho, J.-L. Bredas, P. C. Ewbank, K. R. Mann, *Chem. Mater.* **2004**, *16*, 4436.
[23] H. E. Katz, A. J. Lovinger, J. K. C. Johnson, T. L. W. Siegrist, Y. Lin, A. Dodabalapur, *Nature* **2000**, *404*, 478.
[24] D. M. de Leeuw, M. M. J. Simenon, A. R. Brown, R. E. F. Einerhand, *Synth. Met.* **1997**, 53.
[25] a) B. A. Jones, A. Facchetti, M. R. Wasielewski, T. J. Marks, *J. Am. Chem. Soc.* **2007**, *129*, 15259; b) Z. Wang, C. Kim, A. Facchetti, T. J. Marks, *J. Am. Chem. Soc.* **2007**, *129*, 13362.
[26] S. Handa, E. Miyazaki, K. Takimiya, Y. Kunugi, *J. Am. Chem. Soc.* **2007**, *129*, 11684.
[27] D. G. de Oteyza, E. Barrena, J. O. Osso, H. Dosch, S. Meyer, J. Pflaum, *Appl. Phys. Lett.* **2005**, *87*, 183504.
[28] C. Bossard, S. Rigaut, D. Astruc, M. H. Delville, G. Félix, S. Février-Flandrois, P. Delhaès, *J. Chem. Soc. Chem. Commun.* **1993**, 333.
[29] H. E. Katz, T. Siegrist, J. H. Schön, C. Kloc, B. Batlogg, A. J. Lovinger, J. Johnson, *ChemPhysChem* **2001**, *2*, 167.
[30] Z. Bao, A. J. Lovinger, J. Brown, *J. Am. Chem. Soc.* **1998**, *120*, 207.
[31] J. H. Schön, C. Kloc, Z. Bao, B. Batlogg, *Adv. Mater.* **2000**, *12*, 1539.
[32] R. Ye, M. Baba, Y. Oishi, K. Mori, K. Suzuki, *Appl. Phys. Lett.* **2005**, *86*, 253505.
[33] M.-H. Yoon, C. Kim, A. Facchetti, T. J. Marks, *J. Am. Chem. Soc.* **2006**, *128*, 12851.
[34] W. Y. Tong, A. B. Djurišiæ, M. H. Xie, A. C. M. Ng, K. Y. Cheung, W. K. Chan, Y. H. Leung, H. W. Lin, S. Gwo, *J. Phys. Chem. A* **2006**, *110*, 17406.
[35] J. Yuan, J. Zhang, J. Wang, D. Yan, W. Xu, *Thin Solid Films* **2004**, *450*, 316.
[36] M.-H. Yoon, S. DiBenedetto, A. Facchetti, T. J. Marks, *J. Am. Chem. Soc.* **2005**, *127*, 1348.
[37] B. A. Jones, M. J. Ahrens, M. H. Yoon, A. Facchetti, T. J. Marks, M. R. Wasielewski, *Angew. Chem.* **2004**, *116*, 6523; *Angew. Chem. Int. Ed.* **2004**, *43*, 6363.
[38] A. Facchetti, Y. Deng, A. C. Wang, Y. Koide, H. Sirringhaus, T. J. Marks, R. H. Friend, *Angew. Chem.* **2000**, *112*, 4721; *Angew. Chem. Int. Ed.* **2000**, *39*, 4547.
[39] A. Facchetti, G. R. Hutchison, M. H. Yoon, J. Letizia, M. A. Ratner, T. J. Marks, *Abstr. Pap. Am. Chem. Soc.* **2004**, *227*, U448.
[40] A. Facchetti, M. Mushrush, H. E. Katz, T. J. Marks, *Adv. Mater.* **2003**, *15*, 33.
[41] A. Facchetti, M. Mushrush, M. H. Yoon, G. R. Hutchison, M. A. Ratner, T. J. Marks, *J. Am. Chem. Soc.* **2004**, *126*, 13859.
[42] S. Ando, J. i. Nishida, H. Tada, Y. Inoue, S. Tokito, Y. Yamashita, *J. Am. Chem. Soc.* **2005**, *127*, 5336.
[43] S. Ando, R. Murakami, J. i. Nishida, H. Tada, Y. Inoue, S. Tokito, Y. Yamashita, *J. Am. Chem. Soc.* **2005**, *127*, 14996.
[44] M. H. Yoon, A. Facchetti, C. E. Stern, T. J. Marks, *J. Am. Chem. Soc.* **2006**, *128*, 5792.
[45] J. A. Letizia, A. Facchetti, C. L. Stern, M. A. Ratner, T. J. Marks, *J. Am. Chem. Soc.* **2005**, *127*, 13476.
[46] Y. Wei, Y. Yang, J.-M. Yeh, *Chem. Mater.* **1996**, *8*, 2659.

[47] J. Kong, C. A. White, A. I. Krylov, C. D. Sherrill, R. D. Adamson, T. R. Furlani, M. S. Lee, A. M. Lee, S. R. Gwaltney, T. R. Adams, C. Ochsenfeld, A. T. B. Gilbert, G. S. Kedziora, V. A. Rassolov, D. R. Maurice, N. Nair, Y. Shao, N. A. Besley, P. E. Maslen, J. P. Dombroski, H. Daschel, W. Zhang, P. P. Korambath, J. Baker, E. F. C. Byrd, T. Van Voorhis, M. Oumi, S. Hirata, C.-P. Hsu, N. Ishikawa, J. Florian, A. Warshel, B. G. Johnson, P. M. W. Gill, M. Head-Gordon, J. A. Pople, *J. Comput. Chem.* **2000**, *21*, 1532.
[48] T. Ishiyama, M. Murata, N. Miyaura, *J. Org. Chem.* **1995**, *60*, 7508.
[49] S. Kotha, K. Lahiri, D. Kashinath, *Tetrahedron* **2002**, *58*, 9633.
[50] T. Ishiyama, N. Miyaura, *Chem. Rec.* **2004**, *3*, 271.
[51] D. Enders, O. Niemeier, T. Balensiefer, *Angew. Chem.* **2006**, *118*, 1491; *Angew. Chem. Int. Ed.* **2006**, *45*, 1463.
[52] A. K. Agrawal, S. A. Jenekhe, *Chem. Mater.* **1996**, *8*, 579.
[53] A. Troisi, *Adv. Mater.* **2007**, *19*, 2000.
[54] D. A. da Silva Filho, E.-G. Kim, J.-L. Bredas, *Adv. Mater.* **2005**, *17*, 1072.
[55] K. Tanaka, Y. Matsuura, S. Nishio, T. Yamabe, *Synth. Met.* **1994**, *62*, 97.
[56] J. Naraso, J. i. Nishida, S. Ando, J. Yamaguchi, K. Itaka, H. Koinuma, H. Tada, S. Tokito, Y. Yamashita, *J. Am. Chem. Soc.* **2005**, *127*, 10142.
[57] S. Ando, J. i. Nishida, E. Fujiwara, H. Tada, Y. Inoue, S. Tokito, Y. Yamashita, *Chem. Mater.* **2005**, *17*, 1261.
[58] M. H. Yoon, C. Kim, A. Facchetti, T. J. Marks, *J. Am. Chem. Soc.* **2006**, *128*, 12851.
[59] L. L. Chua, J. Zaumseil, J. F. Chang, E. C. W. Ou, P. K. H. Ho, H. Sirringhaus, R. H. Friend, *Nature* **2005**, *434*, 194.
[60] G. R. Hutchison, M. A. Ratner, T. J. Marks, *J. Am. Chem. Soc.* **2005**, *127*, 2339.

Received: June 4, 2009
Published online: December 28, 2009

